J. Fluid Mech. (1995), vol. 299, pp. 289–331

Vortex intensification and collapse of the Lissajous-elliptic ring: single- and multi-filament Biot-Savart simulations and visiometrics

By VICTOR M. FERNANDEZ[1], NORMAN J. ZABUSKY[1] AND VLADIMIR M. GRYANIK[2]

[1]Department of Mechanical and Aerospace Engineering, Rutgers University, Piscataway, NJ 08855, USA

[2]Institute of Atmospheric Physics, Russian Academy of Sciences, 109017 Moscow, Russia

(Received 8 November 1993 and in revised form 5 May 1995)

The collapsing 'Lissajous-elliptic' (LE) vortex ring is examined via quantifications of *single- and multi-filament* Biot-Savart numerical simulations. In the single-filament simulations, parametric studies show simple relationships between the collapse boundary and the impulse and energy invariants. Collapse becomes *non-monotonic* in time, for a sufficiently small initial core 'radius'. *Self-similar, singular-like* behaviour of the *off-filament* strain-rate growth has been observed in a small interval, just prior to core overlapping. The computation of the strain-rate eigenvalues and vortex stretching in a *diagnostics box* surrounding the collapse region yields patterns observed previously in continuum simulations. New diagnostics are presented, including *line densities* of the energy and the linear and angular momentum, all of which approach zero in the collapse region of the ring. These diagnostics may provide critical parameters for initiating surgery in a topology-changing algorithm. Our multi-filament simulations exhibit layer-like vortex regions and a 'torus'-shaped vortex stretching pattern observed previously in continuum periodic-domain simulations of vortex reconnection. Quantifications in a cross-section of the collapse region indicate that the circulation tends to concentrate in the head or frontside of the convecting dipolar structure. This is also the location of the incipient 'bridge' which is evolving from the weak filaments that have been convected from the initially outer-vortex regions. The formation of this smaller scale vortex structure exhibits the largest vorticity amplification in the variable-core model simulations.

1. Introduction

1.1. *Collapse, reconnection and turbulent intermittency*

Tube-like vortex structures occur in many types of flows and are also predominant in turbulence (Siggia 1981; Kerr 1985; She, Jackson & Orszag 1991; Vincent & Meneguzzi 1991; Douady, Couder & Brachet 1991; Douady & Couder 1993; Jimenez *et al.* 1993; Vincent & Meneguzzi 1994). Interactions between vortex tubes frequently lead to collapse. We define collapse as: the approaching and antiparallel alignment of vortex tubes which results in very large vorticity and strain-rate amplification (Siggia 1985; Siggia & Pumir 1985; Pumir & Siggia 1987; Ashurst & Meiron 1987; Pumir & Kerr 1987; Kida & Takaoka 1988; Meiron *et al.* 1988; Melander & Zabusky 1988; Kerr & Hussain 1989; Zabusky & Melander 1989;

Melander & Hussain 1989; Kida, Takaoka & Hussain 1991; Shelley & Meiron 1991; Zabusky *et al.* 1991; Shelley, Meiron & Orszag 1993; Boratav, Pelz & Zabusky 1992; Kida & Takaoka 1994). The distant approach of wing tip vortices are an example of a collapsing vortex configuration (Crow 1970; Johnston & Sullivan 1994). Experimental realizations of collapse include the high-aspect-ratio elliptic vortex ring (Dhanak & de Bernardinis 1981; Oshima *et al.* 1988), two vortex ring collision (Maxworthy 1972, §6; Fohl & Turner 1975; Oshima & Asaka 1977; Oshima, Noguchi & Oshima 1986: Schatzle 1987; Oshima & Izutsu 1988), the near head-on collision (Smith 1992; Smith & Wei 1994) and the head-on collision of two vortex rings with an instability (Lim & Nickels 1992).

An important experimental and computational aspect of collapse is the growth of strain rate and the consequent vorticity amplification. In his experiments on vortex ring collision, Schatzle (1987) reported a 'dramatic' increase of the strain rate in a short amount of time, followed by a similar decrease as vortex reconnection ends. Confirmation of this behaviour was reported by Winckelmans (1989) in his numerical simulations of the same experiment. The characterization of the strain-rate growth and vorticity amplification is still controversial. In continuum simulations of antiparallel vortex tubes, Pumir & Kerr (1987) find that this type of interaction leads to violent, although not divergent processes. Kerr & Hussain (1989) reported a significant increase in the peak vorticity, consistent with a singularity. Pumir & Siggia (1990) reported faster than exponential growth of vorticity for some initial time interval during collapse, but only exponential at later times. The core deformation during the close vortex interaction was considered the main effect that prevents the singularity formation (Ashurst & Meiron 1987; Pumir & Kerr 1987; Anderson & Greengard 1989; Pumir & Siggia 1990; Shelley & Meiron 1991). In simulations of initially orthogonally offset vortex tubes, Boratav *et al.* (1992) found that the fastest growing local quantity was the squared strain rate ϵ with growth rate at least exponential, but slower than $\exp(\exp(t))$. In simulations of the close interaction of initially antiparallel vortex tubes, Kerr (1993) reported evidence of singular behaviour of the peak vorticity and the peak strain-rate growth. In evolutions from Kida's highly symmetric initial condition, Boratav & Pelz (1994) found that the configuration collapses into a symmetrical hexapole state before reconnection and observe that the evolution of the maximum vorticity during this time scales as $(T - T_c)^{-1}$, where T is the time.

Current research in turbulence examines the nature of vortex structures and interactions (Robinson 1991), including collapse (Zakharov 1988) and the existence of singular solutions of the three-dimensional Navier–Stokes equations (Constantin 1994). However, direct numerical simulations of Navier–Stokes turbulence performed to date have the drawback that the available computer resources limit the resolution, and therefore the Reynolds number obtained in the simulations (She *et al.* 1991). Although low-resolution simulations did not exhibit collapse and reconnection (She, Jackson & Orszag 1990*a*, *b*), recent higher resolution simulations have suggested their presence (Chen & Shan 1992). Yet, collapse reconnection and turbulence exhibit similar behaviour: very large spikes of vorticity (in turbulence called intermittency); alignment of vorticity with the eigenvector of the middle eigenvalue of the strain rate (Ashurst *et al.* 1987; Kerr 1987; Jimenez 1992; Pumir & Siggia 1989, 1990; Boratav *et al.* 1992; Kerr 1993); and coincidence of mean-square strain-rate maxima regions with the alignment regions discussed previously (She *et al.* 1990*b*, 1991). These characteristics lead us to believe that collapse–reconnection can play an important role in intermittency of unforced or weakly forced high Reynolds number phenomena.

1.2. *Filament simulations of collapse*

Numerical simulations of collapsing configurations using vortex filaments have been carried out for a long time. Arms & Hama (1965) applied the Local Induction Approximation equation (LIA) to a study of the evolution of elliptic vortex rings. In this work, Arms & Hama reported that experiments performed with dyed water showed a breakup into two rings (collapse) for the high aspect ratio ellipse. Moore (1972) studied the subsequent nonlinear growth of the disturbance in Crow's instability (Crow 1970). His numerical computation with the regularized Biot-Savart line integral would later be known as the Rosenhead–Moore method. Motivated in part by these works and by the limitations of the local induction approximation, Dhanak & de Bernardinis (1981) conducted numerical simulations of elliptic rings with the Rosenhead–Moore algorithm and found collapse of high aspect ratio rings. In the studies of collapse done by Siggia and Pumir (Siggia 1985; Siggia & Pumir 1985; Pumir & Siggia 1987), faster than exponential growth was found in quantities like curvature, inverse of distance between the filaments, length of filaments and inverse of core radius. However, their late-time results were affected by core overlap and did not properly represent realistic core deformations. Liu, Tavantzis & Ting (1986) studied various configurations with an asymptotic model of vortex stretching. They devoted special attention to the domain of validity of the single-filament results by comparing with Navier–Stokes simulations. Anderson & Greengard (1989) performed multi-filament simulations of two vortex ring collision.

1.3. *Areas covered by this work*

Vortex rings arise in a variety of jet flows of practical interest, including rectangular, square, triangular and cross (Hussain & Husain 1989). The elliptic jet is a flow that has many features in common with the irregular-shaped jets. The elliptic vortex rings that form in this case present a rich panorama of complex behaviours (Hussain & Husain 1989; Husain & Hussain 1993), including the controllable collapse–reconnection phenomenon, as discussed below. In this paper we advocate the experimental and direct numerical study of the parameter space of the 'Lissajous-elliptic', or LE vortex ring, a three-dimensional object with a controllable short-time collapse behaviour, which we have studied using a single-filament Biot-Savart model (Fernandez, Zabusky & Gryanik 1994). Hence we started our studies by re-examining the elliptic vortex ring studies of Dhanak & de Bernardinis (1981).

Siggia and Pumir (Siggia 1985; Siggia & Pumir 1985; Pumir & Siggia 1987) innovatively focused on the singularity problem. They introduced the antiparallel collapse concept and also examined one case of a 'twisted' elliptic vortex ring however, no formula for the initial state was given. In § 2 of this paper, we introduce the Biot-Savart model and the initial conditions corresponding to a twisted or Lissajous-elliptic vortex ring. Section 3 defines some diagnostics for the consistency of the computations and diagnostics for vorticity amplification. Also presented are the practical validity limits of the filament model as reported by Ting & Klein (1991). In § 4, we present parametric studies of the evolution of the LE vortex ring. In § 4.2, we report on the long-time behaviour of the algorithm, where accumulation of numerical error manifests itself through the appearance of a short-wave instability. The results for the collapsing LE vortex ring are presented in § 5. In contrast with previous works, we examine maxima of the strain rate *off the vortex filaments*, as this quantity has been observed to be larger than on the vortex tubes (Zabusky *et al.* 1991; Boratav *et al.* 1992) and its growth is faster than exponential prior to Ting's validity limit of the Biot-Savart model. We also focus on the largest eigenvalue α of the strain-rate matrix, because it coincides with the direction of the 'outgoing' bridges in vortex reconnection (Kida & Takaoka 1987; Zabusky *et al.* 1991; Kida, Takaoka & Hussain 1991; Boratav *et al.* 1992). If a sufficiently small initial core radius is used, the strain-rate diagnostics indicate that collapse becomes *non-monotonic*. Our visualizations of the strain rate and vortex stretching fields present patterns that have been observed previously in continuum simulations of vortex reconnection.

In § 6, initial attempts are made to obtain an asymptotic model for single-filament collapse by applying a self-similarity ansatz to the motion invariants. This procedure suggests that the line densities of linear and angular impulse and energy approach zero in the collapse region of the filament. The numerical results show that the collapse regions on the ring do exhibit motion-invariant densities tending to zero, and indicate that these quantities are appropriate diagnostics for identifying collapsed filament regions in a topological-alteration ('surgery') algorithm.

In § 7, we present multi-filament simulations and observe vortex core flattening. The strain rate and vortex stretching patterns are similar to the ones observed in the single-filament simulations. The vortex stretching function in the multi-filament simulations is closer to the 'torus' shape observed in the continuum simulations (Zabusky *et al.* 1991). The vorticity and strain-rate growth do not saturate in the case of the variable-core model. Finally, in § 8, we present our conclusions.

2. Biot-Savart model, initial conditions and algorithm

For incompressible motion, the velocity field induced by vorticity is given by the Biot-Savart law

$$\boldsymbol{u}(\boldsymbol{x},t^*) = -\frac{1}{4\pi}\int \frac{(\boldsymbol{x}-\boldsymbol{x}')\times\boldsymbol{\omega}(\boldsymbol{x}',t^*)}{|\boldsymbol{x}-\boldsymbol{x}'|^3}\,\mathrm{d}V' . \tag{2.1}$$

The vorticity $\boldsymbol{\omega} = \nabla\times\boldsymbol{u}$ is convected like particles and stretched according to

$$\frac{\mathrm{D}\boldsymbol{\omega}}{\mathrm{D}t^*} = \boldsymbol{\omega}\cdot\nabla\boldsymbol{u} . \tag{2.2}$$

Computing flows with Biot-Savart models is advantageous in that the computational elements can be placed in regions of high 'activity' (vortex stretching) and many fewer test elements can be placed in other regions. Biot-Savart models also allow us to effectively perform inviscid computations with no accumulation of numerical diffusion (Leonard 1980, 1985; Anderson & Greengard 1989).

2.1. *Vortex method*

We use the numerical scheme developed by Knio & Ghoniem (1990) to compute the evolution of a closed tubular vortex region or filament with vorticity

$$\boldsymbol{\omega}(\boldsymbol{x},t^*) = \Gamma\int_C \mathrm{d}\boldsymbol{\chi}(\sigma,t^*)\,f_\delta(|\boldsymbol{x}-\boldsymbol{\chi}(\sigma,t^*)|) , \tag{2.3}$$

where $\boldsymbol{\chi}(\sigma,t^*)$ is the line-axis of the filament of circulation Γ, σ is the initial arc length along the filament and δ is the core radius in the third-degree exponential regularization function

$$f_\delta(\rho) = \frac{3}{4\pi\delta^3(\sigma,t^*)}\exp(\,-\rho^3/\delta^3(\sigma,t^*)\,) . \tag{2.4}$$

This non-compact support regularization function approximates the delta function in the limit of small delta and has second-order accuracy (Beale & Majda 1985). If $\boldsymbol{\omega}$

(2.3) is substituted into the Biot-Savart law (2.1), one obtains the velocity induced by the vortex filament

$$u(x,t^*) = -\frac{\Gamma}{4\pi}\int_C \frac{(x-\chi)\times \mathrm{d}\chi}{|x-\chi|^3}\, g(|x-\chi|), \tag{2.5}$$

where

$$g(\rho) = 1 - \exp(-\rho^3/\delta^3), \tag{2.6}$$

for the third-degree exponential core function f_δ. An integro-differential equation for the curve $\chi(\sigma, t^*)$ representing the filament is obtained in the inviscid case by using the fact that vortex lines are advected as material lines:

$$\frac{\mathrm{d}\chi}{\mathrm{d}t^*} = -\frac{\Gamma}{4\pi}\int_C \frac{(\chi-\chi')\times \mathrm{d}\chi'}{|\chi-\chi'|^3}\, g(|\chi-\chi'|). \tag{2.7}$$

The time-dependent arc length s is defined by

$$s(\sigma,t^*) = \int_0^\sigma \mathrm{d}\sigma' \left|\frac{\mathrm{d}\chi}{\mathrm{d}\sigma'}(\sigma',t^*)\right|. \tag{2.8}$$

2.2. *Initial conditions*

Our initial conditions consist of a vortex filament with circulation Γ, initial core radius $\delta(\sigma, 0) = \delta_0$ and 'Lissajous-elliptic' form (figure 5)

$$(\chi_1, \chi_2, \chi_3) = (a\cos\theta,\ b\sin\theta,\ c\sin 2\theta), \tag{2.9}$$

where $0 \leqslant \theta \leqslant 2\pi$. The grid points are located at equally spaced intervals $\Delta\theta$ or at variable intervals, with the smaller intervals on the collapse region. We call this geometry the 'Lissajous-elliptic' ring, or LE ring, because of its projections on two orthogonal planes. Besides the fact that its parameter space contains cases of very rapid collapse, the low number of parameters of this configuration allows a complete parameter study at less computational expense. The ellipse $c = 0$ presents maximum curvature at $\theta = 0$. At this point the LE ring has curvature

$$\kappa(\theta = 0) = \frac{a}{b^2 + 4c^2}. \tag{2.10}$$

For values of b corresponding to the collapsing high-aspect-ratio ellipse, the maximum curvature becomes so large that its inverse has values close to the vortex core radius. The use of the LE ring with $c > 0$ allows collapsing configurations to be obtained without the high-curvature regions of the original plain ellipse, as can be seen in expression (2.10). High-curvature regions are not desired as they are outside the validity limit of the Biot-Savart model. Another advantage is the antisymmetry, which is exploited to decrease the computational expense of the runs. The amplitude c determines the amount of 'twisting' of the original elliptic ring. The circulation Γ, the geometric parameters a, b, c and the initial core radius δ_0 can be translated into values of the linear impulse, angular impulse and energy invariants. The parameter space is reduced further by choosing the normalizations $\Gamma = 1$ and $a = 1$.

2.3. *Discretization of equations*

Following Knio & Ghoniem (1990) we replace equation (2.7) by

$$\frac{\mathrm{d}\chi_i}{\mathrm{d}t^*} = -\frac{\Gamma}{4\pi}\sum_{j=1}^{N} \frac{(\chi_i-\chi_j)\times \Delta\chi_j}{|\chi_i-\chi_j|^3}\, g(|\chi_i-\chi_j|), \tag{2.11}$$

where the nodes of the filament axis are at $\chi_j = \chi(\sigma_j, t^*)$, with $i = 1, \ldots, N$ and where $\Delta\chi_j$ is the central difference

$$\Delta\chi_j = \tfrac{1}{2}(\chi_{j+1} - \chi_{j-1}) \, . \tag{2.12}$$

Vorticity is automatically updated as the differentials $\Delta\chi_j$ are computed at the new time because material elements obey the same evolution equation as vorticity. For small values of ρ/δ, the factor $g(\rho)/\rho^3$ in (2.11) is evaluated numerically using the Taylor expansion of the function g. Time integration is carried out using a second-order Euler predictor-corrector scheme. In the single-filament runs, we varied the time step systematically to check the convergence of the results. These convergence studies were used in combination with an estimate, presented in § 7, to select the time step for the multi-filament simulations. In the algorithm, by Knio & Ghoniem, variable spatial resolution is achieved by adding new grid points at regions of large filament stretching.

For purposes of adaptive meshing and diagnostics, we measure the quantity

$$q_j = \frac{2\,\delta_j}{h_j} \, , \tag{2.13}$$

which we call the longitudinal 'overlapping' and where $h_j \equiv |\chi_{j+1} - \chi_j|$. If $q = 1$, neighboring vortex elements are just touching. If $q \gg 1$, the discretization approaches the continuum. Convergence of the three-dimensional vortex method, including the filament approach, has been studied by, among others, Beale & Majda (1982), Perlman (1985), Anderson & Greengard (1985) and Greengard (1986). Adequate resolution is obtained with $q \sim 4$ (Knio & Ghoniem 1990). The criteria we use for adding new grid points maintains a prescribed minimum overlapping. The algorithm used to add the new grid points is critical because it may introduce discontinuities in the higher derivatives of the curve. The numerical noise produced by the variable resolution is particularly visible when differentiating the curve to produce graphs of curvature κ and torsion τ, defined in equations (3.1), (3.2), versus s. Although the linear interpolation used by Knio & Ghoniem for introducing new grid points is more economical, in order to obtain smooth diagnostics involving derivatives of the curve χ, we find that a cubic spline interpolation algorithm is essential. An alternative scheme which avoids the evolutionary adaptive mesh is to initially insert many points in what will be the region of collapse, so that at the end of the run, we still have the prescribed minimum resolution with a constant number of grid points. This procedure can be accomplished after the collapse region has been identified in a previous conventional run with variable resolution and therefore involves an iterative process.

We compute with both a constant and a locally variable core. In the latter case we use the volume preserving rule

$$\delta^2(\sigma_j, t^*)\, h(\sigma_j, t^*) = \text{const} \, , \tag{2.14}$$

to control the core radius δ, where h was defined previously. The constant-core model presents smaller variations of energy and linear impulse in the collapse runs (see § 5). At present, there is no rule for varying the core radius that preserves both energy and volume and there is therefore some ambiguity in choosing the proper model. In practice, the characteristics of the variable-core-radius model permit continuation of the collapse computations further to some extent, because the overlapping time t_{ov}, which is the time when the approaching filaments touch for the first time, occurs later. Conversely, short-wave instabilities may develop earlier, as described in § 4.2. In cases with large vortex stretching the conservation of volume is certainly violated by the constant-core model. For long runs without large vortex stretching, it is very important to conserve energy, therefore the constant-core model seems to be more appropriate. For the strain-rate amplification of our single-filament collapsing configurations, there is agreement, up to a reasonable time, between the two models, the variable-core model having only a small variation in the energy at the end of the run.

Finally, we use a dimensionless time (Dhanak & de Bernardinis 1981) defined by

$$t = \frac{t^*}{t_s} = \frac{\Gamma}{4\pi a^2} t^* . \tag{2.15}$$

The strain rate and the vorticity are also non-dimensionalized with the same time scale, $t_s = 4\pi a^2/\Gamma$.

3. Diagnostics

To evaluate the information provided by our numerical simulations, we have implemented two different kinds of measures, one to quantify the quality of the runs and the other to provide physical insight into the processes observed. We introduce the *core-normalized* curvature $\tilde{\kappa}$ and torsion $\tilde{\tau}$:

$$\tilde{\kappa}(s,t^*) = \kappa\,\delta = |\,\boldsymbol{\chi}''\,|\;\delta \tag{3.1}$$

and

$$\tilde{\tau}(s,t^*) = \tau\,\delta = \frac{\boldsymbol{\chi}'\cdot(\boldsymbol{\chi}''\times\boldsymbol{\chi}''')}{\boldsymbol{\chi}''\cdot\boldsymbol{\chi}''}\,\delta , \tag{3.2}$$

where $'$ denotes derivative with respect to s and is computed by approximating $\boldsymbol{\chi}$ with a cubic spline. Plots of curvature and torsion along the filament are especially interesting local diagnostics, because they show any growing instability long before it becomes visible on the ring. We also examine the velocity in the local Frenet–Serret frame

$$(u_{\hat{t}}, u_{\hat{n}}, u_{\hat{b}}) = (\boldsymbol{u}\cdot\hat{\boldsymbol{t}}, \boldsymbol{u}\cdot\hat{\boldsymbol{n}}, \boldsymbol{u}\cdot\hat{\boldsymbol{b}}) , \tag{3.3}$$

where $\hat{\boldsymbol{t}}$, $\hat{\boldsymbol{n}}$ and $\hat{\boldsymbol{b}}$ are the tangent, normal and binormal unit vectors respectively, evaluated also using the cubic spline.

3.1. *Motion invariants*

The motion invariants are global diagnostics which allow evaluation of the numerical computations in terms of their physical validity. Also, the classification of results according to the invariants is more natural than that in terms of the circulation Γ, the geometric parameters a, b, c and the initial core radius δ_0 because of their physical implications. The motion invariants we compute are the linear impulse, the angular impulse and the kinetic energy. Using the filament vorticity distribution (2.3) with any appropriate regularization function yields

$$\boldsymbol{P} = \frac{\Gamma}{2} \int_C \boldsymbol{\chi}\times \mathrm{d}\boldsymbol{\chi} , \tag{3.4}$$

$$\boldsymbol{M} = \frac{\Gamma}{2} \int_C \boldsymbol{\chi}\times(\boldsymbol{\chi}\times \mathrm{d}\boldsymbol{\chi}) , \tag{3.5}$$

$$E = \frac{\Gamma^2}{2} \int_{C'}\int_C \mathrm{d}\boldsymbol{\chi}'\cdot\mathrm{d}\boldsymbol{\chi} \int \psi(|\boldsymbol{x}-\boldsymbol{\chi}'|)\, f_\delta(|\boldsymbol{x}-\boldsymbol{\chi}|)\,\mathrm{d}V , \tag{3.6}$$

where

$$\psi(\rho) = -\int_0^\rho \frac{\mathrm{d}s}{s^2}\int_0^s f_\delta(t)\,t^2\mathrm{d}t + \psi(0). \tag{3.7}$$

Therefore linear and angular impulse are independent of core radius for the regularized filament. In particular, for the LE ring (2.9) we have

$$\boldsymbol{P} = (0,\,0,\,\Gamma\,\pi ab\,), \tag{3.8}$$

$$\boldsymbol{M} = (0,\,0,\,\Gamma\,\frac{3\pi}{4}\,c\,(b^2-a^2)\,). \tag{3.9}$$

We denote the non-zero components of the linear and angular impulse by P and M respectively. Replacing the core function f_δ by the delta function in equation (3.6) results in an approximation (Winckelmans 1989; Winckelmans & Leonard 1993) for the energy

$$E \sim \tilde{E} = \frac{\Gamma^2}{2}\int_{C'}\int_C \mathrm{d}\boldsymbol{\chi}'\cdot\mathrm{d}\boldsymbol{\chi}\;\psi(|\boldsymbol{\chi}-\boldsymbol{\chi}'|)\,, \tag{3.10}$$

which we use throughout this work. Substituting the core function (2.4) in the definition (3.7), we obtain

$$\psi(\rho) = \frac{1}{4\pi}\left(\frac{1-\exp(-\rho^3/\delta^3)}{\rho} + \frac{1}{\delta}\,\hat{\Gamma}\left(\frac{2}{3},\,\frac{\rho^3}{\delta^3}\right)\right), \tag{3.11}$$

where $\hat{\Gamma}$ denotes the incomplete gamma function (Fernandez 1994).

3.2. *Long-time behaviour diagnostics*

The tests to establish the long-time behaviour of the algorithm were made with elliptic rings $c = 0$. For this case, we re-examine three global diagnostics previously employed by Dhanak & de Bernardinis (1981). The first one corresponds to the velocity of the centroid of the ring. The centroid is defined by

$$\bar{\boldsymbol{\chi}} = \frac{\Gamma}{2}\int_C \frac{\boldsymbol{\chi}\times\mathrm{d}\boldsymbol{\chi}\cdot\boldsymbol{P}}{P^2}\boldsymbol{\chi}\,. \tag{3.12}$$

Because of symmetry, the centroid has zero components in the $(\chi_1,\ \chi_2)$ plane. The second diagnostic is the variance

$$\hat{\Sigma} = \frac{1}{2\pi a^3 b}\int_C (\,\chi_1\,\mathrm{d}\chi_2 - \chi_2\,\mathrm{d}\chi_1\,)\,(\,\chi_3 - \bar{\chi}_3\,)^2\,. \tag{3.13}$$

Note that for the elliptic ring ($c = 0$), a perfectly periodic case with period T^* would have minimum variance $\hat{\Sigma}_{min} = 0$ at any $t^* = n\,T^*$. Finally, we check the oscillation period of the ring using Dhanak & de Bernardinis' (1981) expression

$$T^*_{th}(\bar{R},\delta,A) = \frac{8\pi^2\bar{R}^2}{\Gamma}\left[\left\{4\left(\ln\frac{\delta}{\bar{R}} - A\right) + 0.22\right\}\left\{3\left(\ln\frac{\delta}{\bar{R}} - A\right) + 2.23\right\}\right]^{-1/2}, \tag{3.14}$$

obtained from Widnall & Sullivan's (1973) angular frequency for the oscillation of a ring. In this equation, $\bar{R} = (a+b)/2$ and $A = -2.439 \times 10^{-3}$ for our case. The value of A was obtained by comparing the velocity of the circular ring computed numerically with the velocity given by the asymptotic expression obtained by Saffman (1970).

3.3. *Measures of vorticity amplification*

The rate of change of vorticity is given by equation (2.2). Decomposing $\nabla \boldsymbol{u}$ into symmetric and antisymmetric parts, it can be shown (Winckelmans 1989) that

$$\frac{\mathrm{D}\boldsymbol{\omega}}{\mathrm{D}t^*} = \boldsymbol{\omega} \cdot \frac{(\nabla + \nabla^T)}{2} \boldsymbol{u} . \tag{3.15}$$

Therefore, the vorticity amplification depends on the strain-rate tensor

$$\frac{(\nabla + \nabla^T)}{2} \boldsymbol{u}(\boldsymbol{x}, t^*) = \frac{3}{8\pi} \int \frac{\mathrm{D}(\boldsymbol{x} - \boldsymbol{x}')\, \boldsymbol{\omega}(\boldsymbol{x}', t^*)}{|\boldsymbol{x} - \boldsymbol{x}'|^5} \, \mathrm{d}V' = S_{ij} , \tag{3.16}$$

where

$$\mathrm{D}(\boldsymbol{x})\, \mathbf{v} = (\boldsymbol{x} \times \mathbf{v}) \otimes \boldsymbol{x} + \boldsymbol{x} \otimes (\boldsymbol{x} \times \mathbf{v}) , \tag{3.17}$$

with $\otimes$ denoting the dyadic product. For a vortex filament, we use (2.5) and obtain

$$\frac{(\nabla + \nabla^T)}{2} \boldsymbol{u}(\boldsymbol{x}, t^*) = \frac{\Gamma}{8\pi} \int_C \varphi(|\boldsymbol{x} - \boldsymbol{\chi}|)\, \mathrm{D}(\boldsymbol{x} - \boldsymbol{\chi})\, \mathrm{d}\boldsymbol{\chi} = S_{ij} , \tag{3.18}$$

where

$$\varphi(\rho) = -\frac{1}{\rho} \frac{\mathrm{d}}{\mathrm{d}\rho} \left(\frac{g(\rho)}{\rho^3} \right) . \tag{3.19}$$

For the third-degree exponential core function, with g given in equation (2.6), we have

$$\varphi(\rho) = \frac{3}{\rho^2} \left(\frac{1 - \exp(-\rho^3/\delta^3)}{\rho^3} - \frac{\exp(-\rho^3/\delta^3)}{\delta^3} \right) . \tag{3.20}$$

The eigenvalues of the strain-rate matrix obtained from the tensor (3.16) or (3.18) are denoted by α, β and γ with $\alpha > \beta > \gamma$ and, because of incompressibility, $\alpha + \beta + \gamma = 0$. We compute the strain-rate eigenvalues as local diagnostics. Regions with maximum α in the flow may have very large vortex stretching. In some works (Boratav *et al.* 1992) measures of the square strain rate,

$$\epsilon = S_{ij} S_{ij} = \alpha^2 + \beta^2 + \gamma^2 , \tag{3.21}$$

are given as a diagnostic for vorticity growth. We also wish to remark here that the possible breakdown of smooth solutions of the incompressible three-dimensional Euler equations implies that the maxima of both the vorticity and the strain-rate norms grow without bound as the critical time approaches (Beale, Kato & Majda 1984; Ponce 1985).

Large vorticity amplification will only be possible if vorticity coincides in position and direction with regions of large strain rate. To search for these regions, we compute the normalized vortex stretching

$$\frac{1}{|\boldsymbol{\omega}|} \cdot \frac{\mathrm{D}\boldsymbol{\omega}}{\mathrm{D}t^*} = \frac{\boldsymbol{\omega}}{|\boldsymbol{\omega}|} \cdot \frac{(\nabla + \nabla^T)}{2} \boldsymbol{u} , \tag{3.22}$$

and the normalized rate of change of the magnitude of vorticity, given by the quadratic form

$$s_\omega = \frac{1}{\omega^2} \frac{\mathrm{D}\frac{1}{2}\omega^2}{\mathrm{D}t^*} = \frac{1}{|\boldsymbol{\omega}|} \frac{\mathrm{D}|\boldsymbol{\omega}|}{\mathrm{D}t^*} = \frac{\boldsymbol{\omega}}{|\boldsymbol{\omega}|} \cdot \frac{(\nabla + \nabla^T)}{2} \boldsymbol{u} \cdot \frac{\boldsymbol{\omega}}{|\boldsymbol{\omega}|} , \tag{3.23}$$

which also are local diagnostics. Vorticity amplification in terms of stretching of vortex lines is immediately obtained by substituting the definition of a vortex line

$$\frac{\Delta\chi}{|\Delta\chi|} = \frac{\omega}{|\omega|} \tag{3.24}$$

in the right-hand side of equations (3.22), (3.23).

As a geometric measure of collapse, we compute the distance in projection d_m defined by

$$d_m = \min\left\{\left(\chi_1^2 + \chi_2^2\right)^{1/2}\right\}, \tag{3.25}$$

that is, the distance to the axis $(0,0,x_3)$ from the point on the filament closest to this axis. The distance $d_m = d_{min}/2$ because of antisymmetry, where d_{min} is the minimum distance between the collapsing segments of the filament (figure 5). Singular behaviour implies that the interfilament distance must decrease sufficiently rapidly (Fukuyu & Arai 1991). We denote the point on the filament corresponding to d_m by χ_{d_m}. We define the collapsing point χ_c as the material point on the filament corresponding to χ_{d_m} at the overlapping time t_{ov} (i.e. $\chi_c(t_{ov}) = \chi_{d_m}(t_{ov})$). At the overlapping time t_{ov} we have $\delta/d_m = 1$. Note that most of the time $\chi_c \neq \chi_{d_m}$ since χ_{d_m} is not in general a material point. Only as collapse proceeds does the collapsing point χ_c move towards χ_{d_m}.

It has been observed (Zabusky *et al.* 1991; Boratav *et al.* 1992) that the strain-rate amplification during collapse–reconnection is maximum off the vortex tubes. This motivates us to search this field in the surroundings of our vortex filaments. To accomplish this task, we proceed in two ways. One is to compute the maximum α_m of the largest strain-rate eigenvalue α (3.16) on the axis $(0,0,x_3)$ for $x_3 \geqslant \chi_{3d_m}$. We choose this axis because the filament collapses towards it. The upper part is chosen because it is in this region, above the filaments, where bridge formation takes place during vortex reconnection. The other way is to compute the vorticity amplification diagnostics on the filament and also in a *diagnostics box*, which covers some neighbourhood of the filament segment containing the point χ_{d_m}, or the point detected as having the largest stretching according to (3.23). This automatically finds any collapsing region, if one is present. The diagnostics box is shown in figure 12 for the last time computed of the collapsing LE ring with initial core radius $\delta_0 = 0.07595$.

3.4. *Limits of validity of the filament approach*

The filament vorticity distribution given by (2.3) assumes a core structure that does not change in time. This assumption is valid when the core radius $\delta(\sigma, t)$ is much smaller than any other length scale in the flow (Ting & Klein 1991; Leonard 1985). Conversely, we know that, in fact, very closely interacting vortex tubes suffer large core distortion (Ashurst & Meiron 1987; Pumir & Kerr 1987; Anderson & Greengard 1989; Pumir & Siggia 1990; Shelley & Meiron 1991; Zabusky *et al.* 1991; Kida *et al.* 1991; Boratav *et al.* 1992). Practical limits of validity for the filament model have been reported by Ting & Klein (1991) to be

$$\frac{R_{min}}{\delta} \geqslant k_1 = 2 \quad \text{and} \quad \frac{d_{min}}{2\delta} \geqslant k_2 = 1.5, \tag{3.26}$$

where R_{min} is the minimum radius of curvature of the filament and d_{min} is the minimum distance between two distinct points of the filament that have the same core radius. These values for k_1 and k_2 were verified (Ting & Klein 1991) by a comparison of numerical results obtained using an asymptotic model with vortex stretching with numerical solutions of the Navier–Stokes equations. These values are moderate in

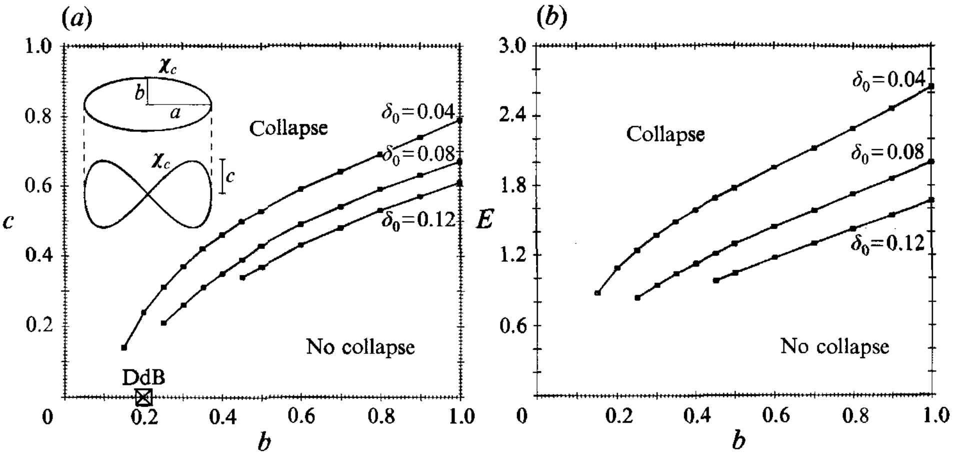

FIGURE 1. Parameter space of the Lissajous-elliptic (LE) vortex ring with the normalizations $\Gamma = 1$ and $a = 1$, in terms of (*a*) the geometry and (*b*) the energy and linear impulse. The curves are the collapse boundaries for three different initial core radii. The elliptic vortex ring study by Dhanak & de Bernardinis is marked with DdB.

that the difference between asymptotic and numerical solutions remains less than 2% if these particular values of k_1 and k_2 are chosen (Ting & Klein 1991).

4. Parameter study

After reducing the parameter space with the normalizations $\Gamma = 1$ and $a = 1$, the parameters to be explored are b, c and the initial core radius δ_0. In terms of the motion invariants, if a is constant, the non-zero component of the linear impulse P is proportional to b and independent of c, as can be seen in equation (3.8). Therefore, the impulse of the ring is equivalent to b. In figure 1, we see the regions corresponding to the different types of evolution of the LE ring. The first region has periodic or nearly periodic oscillations and is characterized by small values of c and values of b close to 1. The form of such vortex rings is close to a low-aspect-ratio ellipse. The second type of region corresponds to values of the geometric parameters that produce regions of high normalized curvature (3.1), either initially or almost immediately after the initial time. We call these regions 'local collapse' regions and they appear at the lower left, for small values of b and c. These rings are close to high-aspect-ratio ellipses. The LE ring also presents a region of 'non-local collapse' as discussed below.

4.1. *Collapse region in the parameter space*

Non-local collapse occurs when two opposite segments of the vortex filament form an antiparallel approaching configuration (figure 5). The boundary of this collapse region is marked in figure 1 for three different initial core radii δ_0. We observe that for any given value of $b > 0.3$, the non-local collapse boundary can be crossed by increasing c (figure 1*a*). For a smaller initial core radius, the collapse boundary shifts towards higher values of c. The corresponding shift of the collapse boundary in the energy graph shows that for a smaller initial core radius, higher levels of energy are required for collapse (figure 1*b*). Finally, between the collapse and non-collapse regions, there is a narrow region, not shown in figure 1, with *non-monotonic* collapse that we call the 'bounce' region. The bounce process can also be generated by taking a set of geometric parameters in the collapse region and decreasing the initial core radius while keeping the other parameters constant. This causes the collapse boundary to shift upward, leaving the point, defined by the geometric parameters kept constant, in the bounce region. We show this sequence of parameter variation in § 5. The change in initial core radius represents a fundamental change in the initial conditions because the collapse boundary is shifted, which may be a consequence of changing the energy balance on the ring. The region of the parameter space corresponding to the elliptic vortex ring ($c = 0$), explored previously by Dhanak & de Bernardinis (1981), is also indicated in figure 1. They found non-local collapse for $b = 0.2$ which corresponds to a high-aspect-ratio ellipse. A potentially useful case that could be compared with other types of analysis and experiments of collapse is the 'Lissajous-circle', in which $a = b = 1$ (Fernandez *et al.* 1994). The remaining free parameters in this case are c and the initial core radius δ_0. In terms of the motion invariants, the linear impulse $\boldsymbol{P}$ and the angular impulse $\boldsymbol{M}$ are now constant parameters. In particular, $\boldsymbol{M}$ is the null vector.

In the next sections we present in more detail the results in two additional regions of the parameter space. The first corresponds to the periodic or nearly periodic region, and the second corresponds to the non-local collapse region with its transition to bouncing.

4.2. *Long-time behaviour: Widnall's instability*

The region in the parameter space corresponding to the low-aspect-ratio ellipse presents a periodic or near-periodic oscillating evolution of the vortex ring, with the period given by (3.14). This is a good test case for the algorithm, and in particular for its long-time behaviour. We use the elliptic ring with $\Gamma = 1, a = 1, b = 0.8, c = 0$ and the initial core radius $\delta_0 = 0.126$ and perform runs with the adaptive mesh and both the constant- and variable-core models. By varying the numerical parameters, we find that the overlapping q, defined in equation (2.13), governs the nature of the long-time behaviour. We examine first the results with the constant-core model. We observe (table 4.1 in Fernandez 1994) that, after starting with a low overlapping, quantities like the mean velocity of the centroid $\bar{u}$, the minimum variance $\hat{\Sigma}_{min}$ and the oscillation period T, all computed using five periods of oscillation of the ring, show convergence as q increases. For values of minimum overlapping along the ring $q_{min} < 10$, the algorithm is able to compute up to 24 periods of oscillation, which is equivalent to ~12 000 Δt time steps, with $\Delta t = 2.0 \times 10^{-3}$. For $q_{min} > 10$, as the number of grid points is increased, a deterioration in the numerical accuracy manifests itself by a breakdown of the algorithm at an earlier time, which is also registered by the destruction of the convergence. Similar behaviour has been reported for the Rosenhead–Moore algorithm (Hon & Walker 1988). The nature of the breakdown is shown in figure 2. In figure 2(*a*), we can see the top view of the vortex ring at the initial time, at 5.5 periods of time and at the breakdown time. At this final time, an $m = 10$ mode is visible on the ring. In the graph of the velocity of the centroid, defined by (3.12) and presented in figure 2(*b*), we observe a regular and clean behaviour up to 5 or 5.5 periods of oscillation of the elliptic ring. The graph of the variance $\hat{\Sigma}$, which is defined by (3.13) and presented in figure 2(*c*), has similar behaviour. At this stage of the computation ($t \sim 5$), the period of oscillation computed numerically is $T = 0.9744$ for $n_0 = 256$ grid points which, when compared with the theoretical value of $T^*_{th}/t_s = 0.95951$, given by (3.14) and the normalization (2.15), shows a difference of about 1.6%. At 5.5 periods, we observe in the graphs of the velocity of the centroid and the variance the appearance of a long-wave mode superposed to

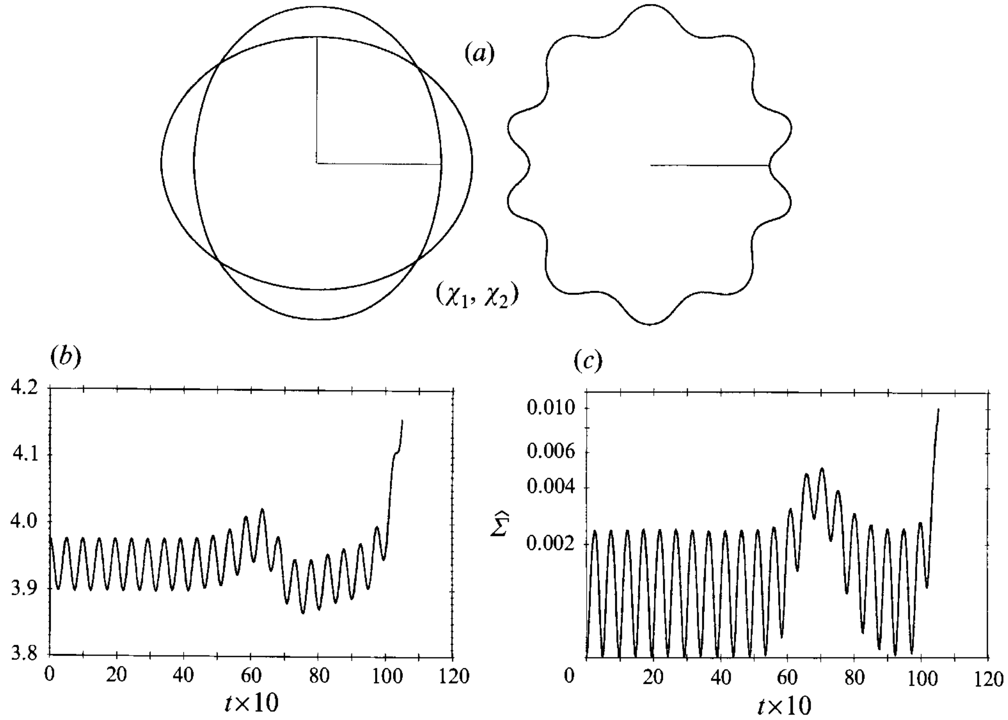

FIGURE 2. Algorithm long-time behaviour in the periodic regime. (*a*) Top view of the ring at times $t = 0$, 5.34 (5.5 periods) and 11.97. Also shown (*b*) the velocity of the centroid and (*c*) the variance $\hat{\Sigma}$ *vs.* time t. The vortex ring parameters are $b = 0.8$, $c = 0$ and $\delta_0 = 0.126$. The time step is $\Delta t = 2.0 \times 10^{-3}$, the minimum initial overlapping is $q_{min} = 10.27$ and the maximum initial normalized curvature is $\tilde{\kappa}_{max} = 0.197$.

the original oscillations. Nevertheless, no sign of the perturbation can be seen on the ring (figure 2*a*) at this time. For $t \sim 11$, the computation breaks down for numerical reasons, as seen in the graphs of the velocity of the centroid and the variance. The $m = 10$ mode, visible on the ring at the final time shown, is consistent with the linear theory by Widnall *et al.* (Widnall & Sullivan 1973; Widnall, Bliss & Tsai 1974) for the case of the 'spurious' short wave, and is independent of time step and machine precision (table 4.1 in Fernandez 1994), although it seems to need enough spatial resolution to develop ($q_{min} \sim 10$). Lower resolution seems to have a smoothing effect, since these cases break down much later in time, as mentioned previously, through the appearance of smaller, non-smooth 'wiggles'.

A closer look into the $m = 10$ mode can be obtained by considering the overlapping q and the normalized curvature $\tilde{\kappa}$ and torsion $\tilde{\tau}$, given by (2.13), (3.1) and (3.2), *vs.* the arc length s along the vortex ring. These quantities are plotted in figure 3 for the time at 5.5 periods ($t = 5.34$). We see that even though the ring, top and side views of which are also shown, does not have visible traces of the $m = 10$ mode, they are clearly present in the derivatives of the curve as shown by the overlapping and the normalized curvature and torsion. They are also present in the normalized rate of change of the magnitude of vorticity s_ω, defined by (3.23), on the filament and the energy density, which we do not show for this case and which we introduce later. At the breakdown time, presented in figure 4, the $m = 10$ mode is visible on the filament. The derivatives now show that the regular waves observed in the previous

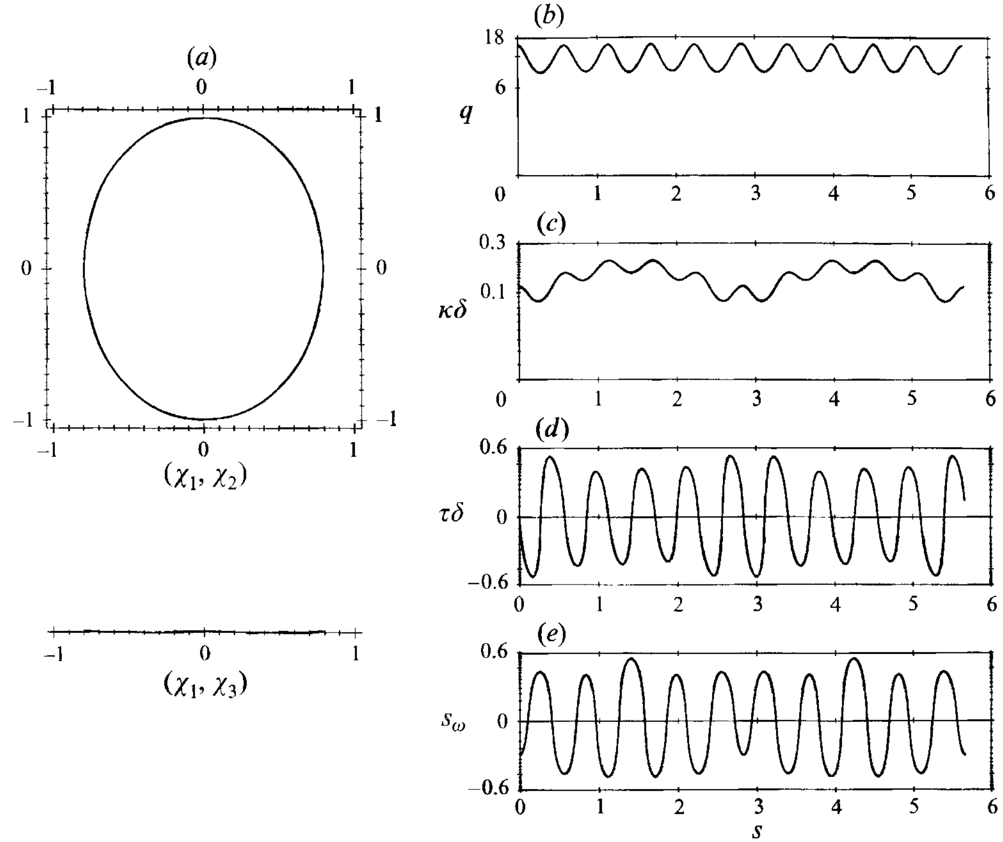

FIGURE 3. (*a*) Top and side views of the elliptic ring at 5.5 periods ($t = 5.34$). The $m = 10$ mode, not visible on the ring, is present in the graphs of (*b*) the overlapping q, (*c*) the normalized curvature $\tilde{\kappa}$, (*d*) the normalized torsion $\tilde{\tau}$ and (*e*) the normalized rate of change of vorticity magnitude s_ω *vs.* arc length s.

picture have evolved by this time into a ten-spikes pattern. Irregularities are also present in the rate of change of the magnitude of vorticity s_ω. The blow up in the local curvature visible in the ten spikes of this graph is an example of 'local collapse'. By this time, the curvature validity limit of the Biot-Savart model in (3.26) has been largely violated. Local collapse has been studied recently by Klein & Majda (1991) for the case of a perturbed helical vortex filament, using an asymptotic filament equation with self-stretching (see also Klein & Knio 1995). For this constant-core case, the changes in impulse and energy at the end of the run were about -1.6% and -1.07% respectively. The variable-core-radius model also produces the $m = 10$ mode, but this one develops earlier. For this case, the waves are visible after the third period of oscillation of the elliptic ring. Conversely, changes in impulse and energy are considerably larger than those obtained in the constant-core-radius model. Knio & Ghoniem (1990) have performed studies of the instability of the circular ring using the same algorithm and have shown the same unstable mode. In contrast with the present work, however, they do not have a second harmonic, i.e. the oscillating elliptic ring, and they introduce an initial perturbation. The only perturbation we have is error, from which the Biot-Savart model picks up the most unstable mode. Even though the $m = 10$ mode appears in a very consistent and smooth manner, it

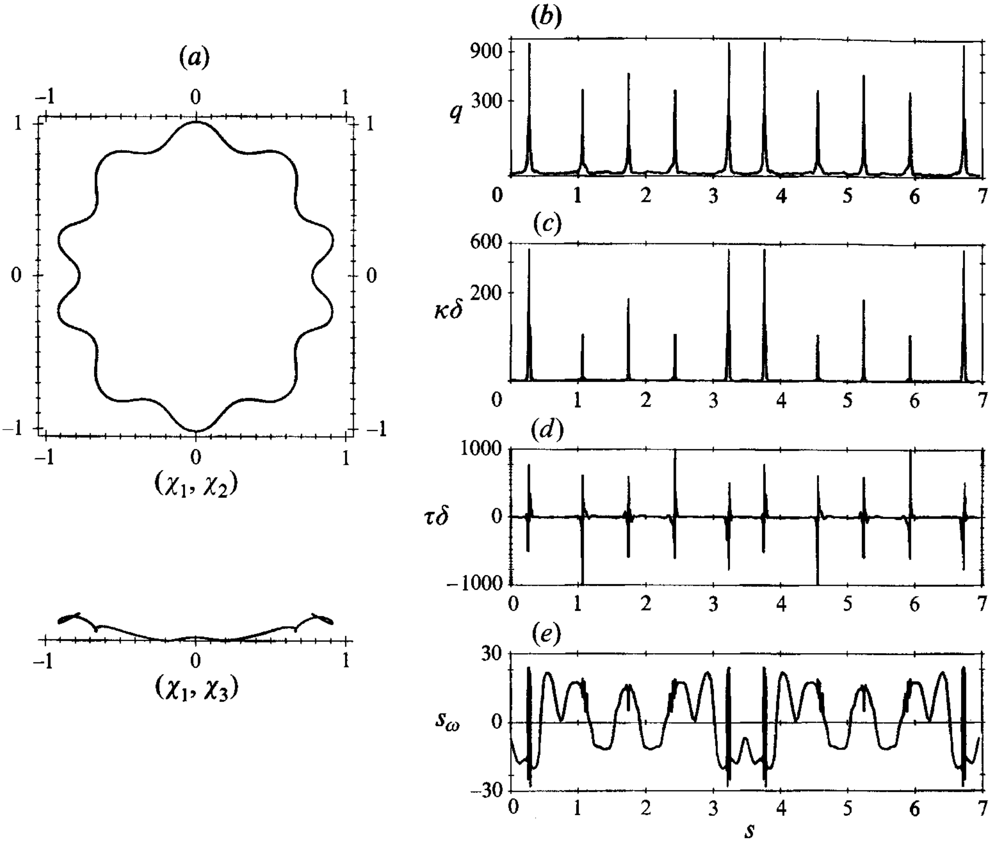

FIGURE 4. (*a*) Top and side views of the ring at breakdown time $t = 11.97$. The $m = 10$ mode has become visible on the ring. In the graphs of (*b*) overlapping q, (*c*) normalized curvature $\tilde{\kappa}$ and (*d*) normalized torsion $\tilde{\tau}$ the ten waves have evolved into a ten-spikes pattern. The graph (*e*) with the normalized rate of change of vorticity magnitude s_ω also shows irregular behaviour.

is outside the range of validity of the Biot-Savart model because the wavelength of this mode is of the order of the core radius. Therefore we should expect distortions of the core structure, which we cannot simulate with this model.

Our studies with the low-aspect-ratio elliptic ring have shown the breakdown characteristics of the algorithm we are using. We have learned that well-resolved runs in space and time will break down through the appearance of short waves. The perturbation that feeds this instability is numerical and has an impact mainly on the long-time behaviour of the algorithm. We are interested in the study of collapsing configurations. Collapse phenomena involve such short developing times that these long-time behaviour effects become unimportant. Long-time behaviour effects may start appearing only if the collapse parameters are changed so that collapse is delayed, but, even in this case, through the studies just presented, we have gained some knowledge that allows us to identify these effects.

5. Collapse of the Lissajous-elliptic ring

The collapsing LE vortex ring is presented in figure 5, where we show the projections of the ring on orthogonal planes at different times. The parameters of this run, designated as the 'bounce case', are $\Gamma = 1$, $a = 1$, $b = 0.4$, $c = 0.5$ and initial core

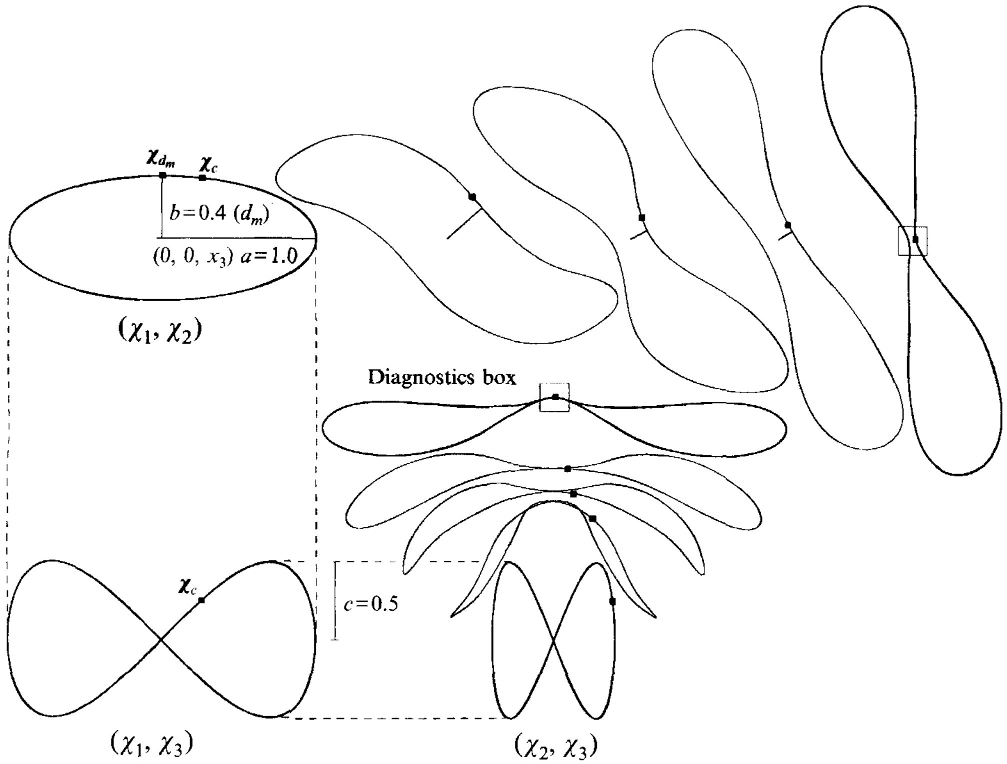

FIGURE 5. Lissajous-elliptic (LE) vortex ring projections onto orthogonal planes at different times in its evolution towards collapse. The times presented are $t = 0$, 0.045, 0.09, 0.135 and 0.18. Also represented are the point χ_{d_m}, closest to the axis $(0, 0, x_3)$ and the collapsing point χ_c. The ring parameters are $b = 0.4$, $c = 0.5$ and $\delta_0 = 0.02$, with the variable-core model. The time step is $\Delta t = 10^{-5}$, the minimum initial overlapping $q_{min} = 5.42$ and the maximum initial normalized curvature $\tilde{\kappa}_{max} = 0.0792$. Position of projections does not correspond to actual motion of the ring.

radius $\delta_0 = 0.02$. This filament was discretized initially with $n_0 = 1600$ grid points. This run was performed with the alternative scheme, i.e. no addition of new grid points, but with an initially higher density of grid points on the collapsing segments of the ring. The time step was $\Delta t = 10^{-5}$. The initial minimum overlapping and maximum normalized curvature are $q_{min} = 5.42$ and $\tilde{\kappa}_{max} = 0.0792$ respectively. Runs performed at various spatial and temporal resolutions indicated convergence of the results. The amount of twisting of the ellipse, specified by the c value, corresponds to an orthogonally offset configuration in the (χ_1, χ_3) projection (figure 5). As time elapses, the ring with the initial orthogonal offset moves towards the antiparallel configuration characteristic of collapse. The computation is stopped at the overlapping time t_{ov} where $d_m/\delta = 1$, which occurs just beyond the time $t = 0.18$ presented in figure 5. The overlapping time for the computation on the figure is at $t_{ov} \sim 0.1814$. The validity limit $d_m/\delta = 1.5$, as given by (3.26), is reached at $t \sim 0.1806$, also after the last time shown in figure 5, which corresponds to a computation with the variable-core model and the smallest initial core radius presented in this paper. The figure for the constant core model presents no visible differences. The use of the variable-resolution algorithm does not show significant changes in the diagnostics that follow, except in the graphs of curvature and torsion (figure 7), where non-smooth behaviour is observed in the regions of the filament where the new grid points have been added.

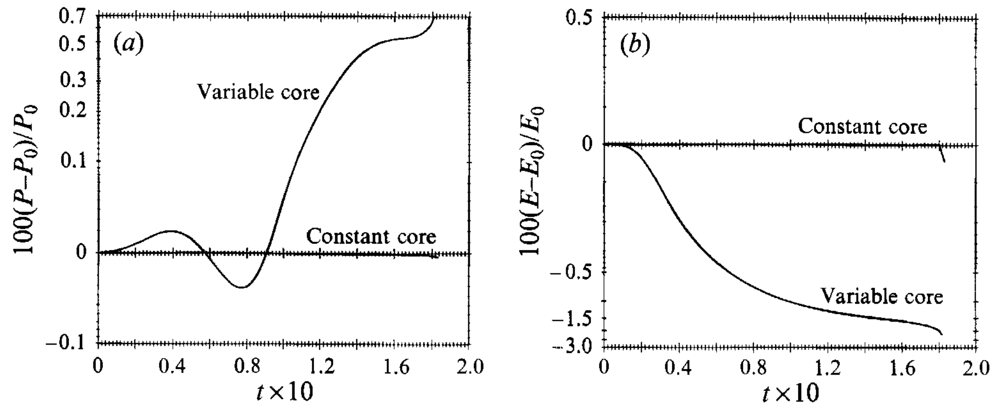

FIGURE 6. Time evolution of (*a*) the non-zero component of linear impulse P and (*b*) the energy E of the collapsing ring in figure 5 for the constant- and variable-core models.

5.1. *Energy and impulse*

For the run just described, which is the most significant of our series, we present now in figure 6 the computed percentage change of the non-zero components of linear impulse P and of the energy E defined by equations (3.4) and (3.10), which represent a measure of the quality of the runs from a physical point of view. The graphs are for both constant- and variable-core models. For constant core, the computed variations of linear impulse and energy are less than 0.01% and 0.05% respectively at the end of the run. For variable core, the change in linear impulse is less than 1% and the change in energy is less than 3% at the end of the run.

5.2. *Curvature, torsion and stretching near collapse*

Other measures of the quality of the collapse computation are presented in figure 7. This figure shows the overlapping of vortex elements q, the normalized curvature $\tilde{\kappa}$, the torsion $\tilde{\tau}$ and the normalized rate of change of the magnitude of vorticity s_ω, given respectively by (2.13), (3.1), (3.2) and (3.23), *vs.* arc length s. The corresponding time in the evolution of the ring is $t = 0.18$. The origin in all of these plots is at the value of s for the point χ_{d_m} which, at overlapping time t_{ov}, is the collapsing point χ_c. The graph of the overlapping shows adequate resolution up to this time. The normalized curvature graph indicates no regions of large normalized curvature, which means we are still inside the regime of validity of the Biot-Savart model. The torsion graph shows that even higher derivatives of the filament, computed numerically, are still well behaved, even though they have some noise in the form of very short waves. The two peaks in the torsion are produced by the curvature minima that can be seen in figure 7(*c*). The rate of change of the magnitude of vorticity s_ω shows two maxima corresponding to the collapsing regions of the ring. The plots correspond to the run with no variable resolution (same as in figure 5), which results in considerably reduced levels of noise in curvature and torsion, in comparison with the run with variable resolution.

5.3. *Dependence of the strain-rate growth on the core radius*

For the circulation Γ and the geometric parameters a, b and c of the initial condition presented in figure 5, we computed the evolution of rings with different initial core radii. We changed the initial number of grid points n_0 in order to keep the initial minimum overlapping $q_{min} > 4$. The strain rate α_m was measured on the upper axis

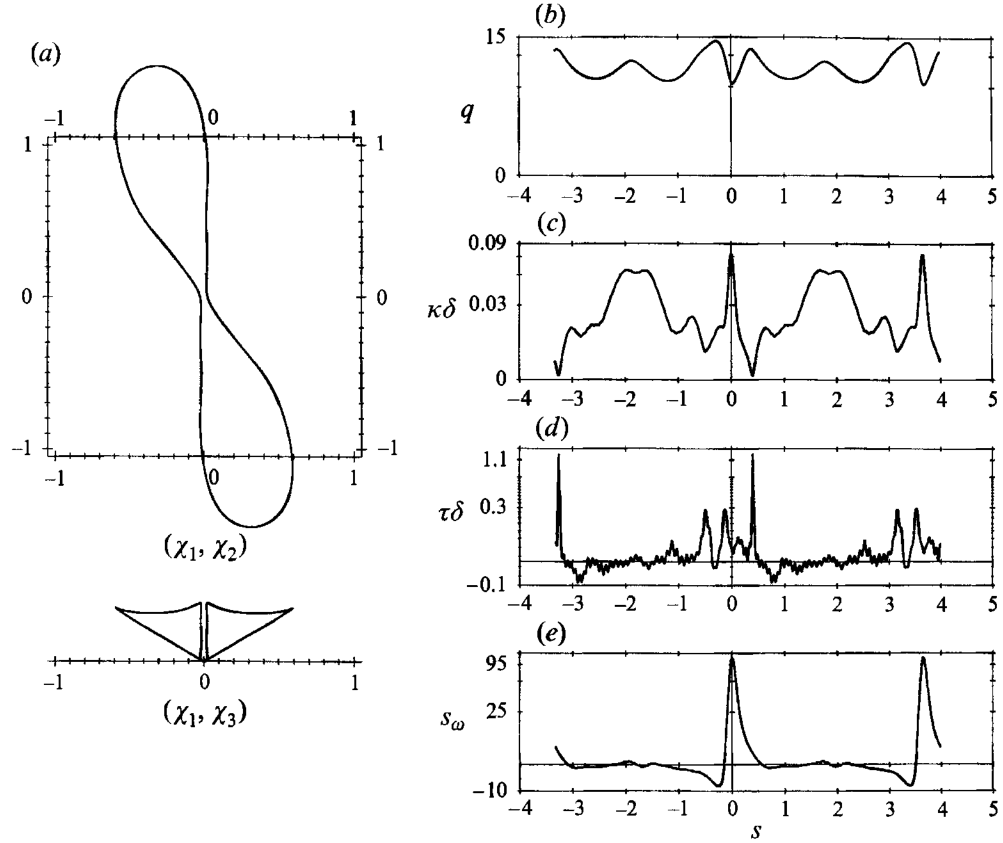

FIGURE 7. (*a*) Top and side views of the collapsing ring in figure 5 at $t = 0.18$. Also included are graphs of (*b*) overlapping q, (*c*) normalized curvature $\tilde{\kappa}$, (*d*) normalized torsion $\tilde{\tau}$ and (*e*) normalized rate of change of vorticity magnitude s_ω *vs.* arc length s. The origin $s = 0$ is at the point χ_{d_m}.

$(0, 0, x_3)$ as explained in § 3. These runs were done with the variable-core model (2.14). The stop time for the computations is the point at which the filaments touch for the first time, which corresponds to $\delta / d_m = 1$. As we decrease the initial core radius from $\delta_0 = 0.07595$ to 0.03, all of the α_m curves monotonically increase with time. The collapse time decreases while the strain rate increases, as expected, when a smaller initial core radius is chosen. The inverse of the distance d_m normalized with the core radius δ is also monotonic in its evolution towards collapse.

As we continue decreasing the core radius from $\delta_0 = 0.03$ to 0.02, the collapse time inverts its previous behaviour and starts increasing, which can be seen in figure 8(*a*) for the strain rate α_m. All of the curves presented are for the variable-core model except the dashed one, which is for the constant core model. The non-monotonic behaviour occurs for both variable- and constant-core models, as can be observed by comparing the dashed curve with the continuous line for the initial core radius $\delta_0 = 0.02$. The variable-core curve for this initial core radius corresponds to the evolution of the ring shown in figure 5. We can reduce the collapse time again by increasing the aspect ratio of the ring as shown by the curve with $b = 0.2$. In figure 8(*b*), the graph for the inverse of the normalized distance δ / d_m, it can be seen that, as the initial core radius is decreased, an interval of time appears in which the evolution towards collapse stops. In fact, it even reverses for a while for the

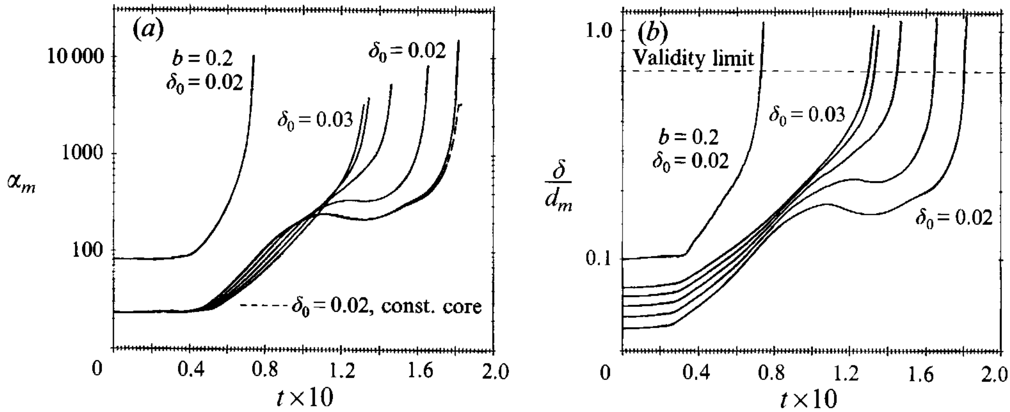

FIGURE 8. (*a*) Maximum strain-rate eigenvalue α_m in the upper axis $(0, 0, x_3)$ and (*b*) inverse normed distance δ/d_m *vs.* time t, for the variable-core model with $b = 0.4$, $c = 0.5$ and core radii $\delta_0 = 0.03$, 0.0275, 0.025, 0.0225, and 0.02. The dashed line corresponds to the constant core model with $\delta_0 = 0.02$. Also included is a curve for a higher-aspect-ratio Lissajous-ellipse with $b = 0.2$, $c = 0.5$ and $\delta_0 = 0.02$. Figure 5 corresponds to the non-monotonic evolution with $\delta_0 = 0.02$ and the variable-core model.

smaller initial core radii. After this 'bounce back' interval of time, collapse resumes. The elimination of the bounce back effect can be achieved by choosing a higher aspect ratio, as mentioned before. In figure 8 we also mark the validity limit of the Biot-Savart model given by (3.26).

5.4. *Quantification of strain-rate eigenvalue intensification*

To characterize the observed strain-rate growth, we fitted the results presented in figure 8(*a*), for the variable-core model with $\delta_0 = 0.02$, with a functional form $\tilde{\alpha}_m$ representing the data, which, since there is no theory, we arbitrarily choose as

$$\tilde{\alpha}_m = \frac{a_c}{t_c - t} + b_c \ln(t_c - t) + c_c + d_c t \,. \tag{5.1}$$

The fits were done alternatively with $d_c = 0$, which corresponds to the function without the linear term, and $b_c = 0$, which corresponds to the function without the logarithmic term. To find the parameters t_c, a_c, c_c and b_c or d_c, we first fit a fifth-order polynomial to α_m^{-1}, which is shown in figure 9(*b*). We then extrapolate the value of the time t_c where α_m^{-1} is zero. Once we have the collapse time t_c, we fit α_m to obtain the rest of the parameters of the function $\tilde{\alpha}_m$. The curve fittings are done using a standard package subroutine (MINPACK), which fits nonlinear curves by least-squares using a modified Levenberg–Marquardt algorithm. The fitting region is selected as follows. We choose the final-time end according to the validity limit (3.26); we then fit regions with different lower-time ends until we obtain the best parameters in terms of the Euclidean norm of the difference between experimental and fitted points $\| \alpha_m - \tilde{\alpha}_m \|$. The best fits are, for $b_c = 0$, $(t_c, a_c, c_c, d_c) \sim (0.181581, 59.1, -379.6, 688.6)$ and, for $d_c = 0$, $(t_c, a_c, b_c, c_c) \sim (0.181614, 63.0, 83.7, 193.3)$. Notice that the difference in the values of a_c corresponding to these curve fittings is only 6%. The last fit, obtained for the function including the logarithmic term, is slightly better. This fitting was performed using 101 sampling points, spaced every 30 time steps ($\Delta t = 10^{-5}$), corresponding to the time interval $0.1503 \leqslant t \leqslant 0.1806$. At the lower bound of the interval, the distance between the collapsing portions of the filament is $2d_m/\delta \sim 11$ core radii. Notice that, because $b_c > 0$ in this fit, the logarithmic term reduces the

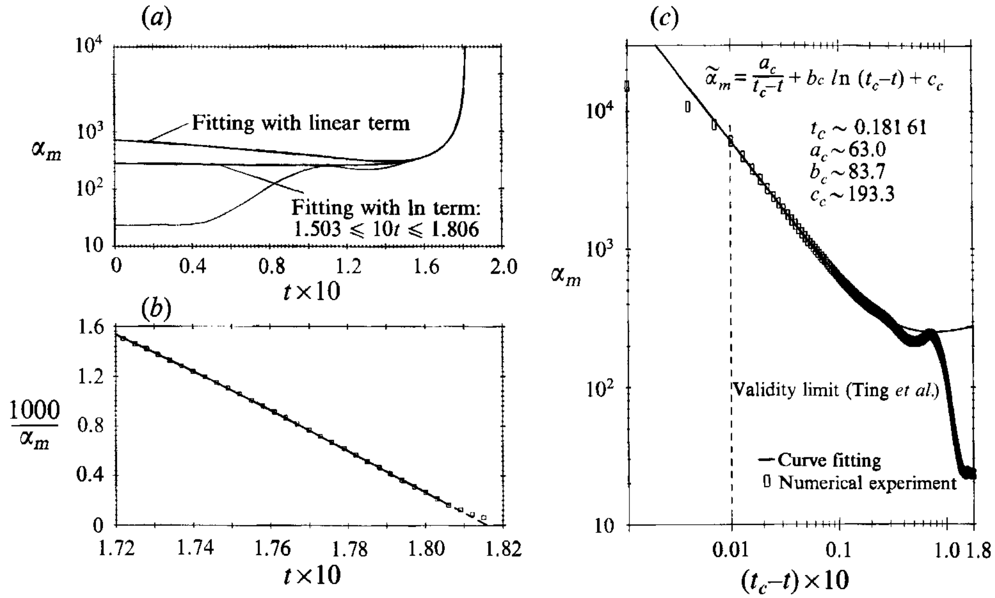

FIGURE 9. (*a*) Fitting of the strain-rate eigenvalue α_m for the evolution of the ring in figure 5. (*b*) The collapse time t_c is obtained from extrapolation (dashed line) of the inverse of α_m. (*c*) Fitting, in log-log scales, of the function $\tilde{\alpha}_m$ with the logarithmic term. The Euclidean norm of the difference $(\alpha_m - \tilde{\alpha}_m)$, between experimental and fitted points, divided by the number of points in the fitted interval, is fnorm/m = 0.427493.

growth of α_m. The results of the fit can be seen in the original semi-logarithmic scales in figure 9(*a*), and also in log-log scales in figure 9(*c*). In the graph with the log-log scales, the time variable has been changed to $(t_c - t)$ so that collapse now progresses towards the left. The last point of the numerical results in the plot corresponds to t_{ov}. In figure 9(*c*), it can be seen that there is a region of the experimental points behaving according to the functional form (5.1) used for the fitting. Near collapse, the deviation of the experimental points from the fitting starts after the validity limit of the Biot-Savart model is passed. It can also be observed that the first singular term becomes dominant only as the validity limit of the model is approached, indicating that the self-similar regime for this model is small. The fitting region, chosen as explained before, leaves out the last computed points which, beyond the validity limit of the model, show a tendency towards saturation.

5.5. *Magnitude and alignment of vorticity on the filament*

In figure 10 we plot, in semi-logarithmic scales, the maximum of the vorticity magnitude $|\omega|_{max}$ on the filament for the variable- and constant-core models, and the vorticity magnitude $|\omega_c|$ at the collapsing point χ_c for the variable-core model. For this last case, we observe qualitatively in the figure that the maximum of the vorticity magnitude and the vorticity magnitude at the collapsing point exhibit faster than exponential growth. The constant-core model exhibits an unphysical constant maximum vorticity magnitude, even though this model shows the same strain-rate intensification behaviour as the variable-core model (see figure 8). An important question we cannot answer with the single-filament Biot-Savart model is whether or not the evolution of the strain rate and vorticity in the close vortex interaction saturates or continues its near singular behaviour. In recent work by Kerr (1993) the presence of singular

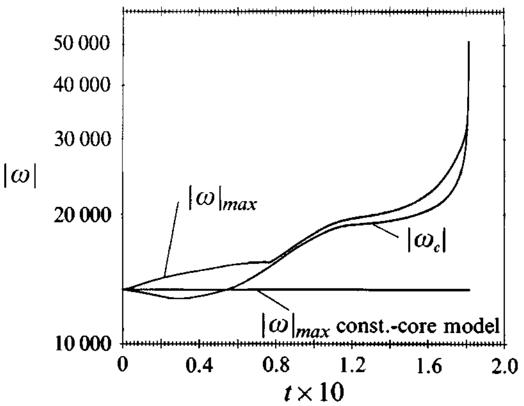

FIGURE 10. Evolution of the vorticity magnitude $|\omega|$ on the filament for the initial conditions in figure 5, with the variable- and constant-core models.

behaviour during the close interaction is suggested. This author reports that the peak vorticity and the peak axial strain-rate component, which is aligned with vorticity, have faster than exponential growth: ω_p and $e_{yy,p} \sim 1/(t_c - t)$ in agreement with self-similarity.

As mentioned in the introduction, the alignment of vorticity with the eigenvector of the middle strain-rate eigenvalue β has been reported for vortex reconnection (Pumir & Siggia 1989, 1990; Boratav *et al.* 1992; Kerr 1993). In figure 11 we show the evolution in time of the absolute value of the dot product $\hat{e}_\beta \cdot \omega/|\omega|$. This dot product was computed at the collapsing point χ_c of the LE ring in figure 5 with different core radii. We observe that, as time progresses, this value in fact tends to 1 for all core radii. For the bounce case, $\delta = 0.02$, this occurs relative early in time, with the bounce effect in the form of a valley at about $t = 0.11$. It has been argued (Jiménez 1992), that the observed alignment is a consequence of the formation of two-dimensional vortex configurations. Figure 11 is consistent with this idea, as it shows the evolution of the collapsing segments of the filament towards the nearly two-dimensional, antiparallel configuration, which is reached relative early in time for the bounce case.

5.6. *Strain rate and vortex stretching field visualizations*

Direct visualization of the three-dimensional fields seems to be the most efficient way to capture spatial coherence (She *et al.* 1990*b*). We produced pictures of the strain rate and vortex stretching fields in the diagnostic box, introduced in §3, surrounding the collapse region (figure 12). Figure 13 shows isosurfaces of the eigenvalue α at 80% of the maximum in the diagnostics box for the times $t = 0.18$, 0.1807 and 0.1814. The data correspond to the bounce case presented in figures 5 and 9. The maximum in the box increases with time. The filaments shown have one fifth of the actual core radius. The first time (figure 13*a*) corresponds to a distance of $2d_m/\delta \sim 3.7$ core radii between centerlines; the next time (figure 13*b*) is close to the validity limit $d_m/\delta \sim 1.5$, given by equation (3.26), which occurs at $t \sim 0.1806$; the last time shown (figure 13*c*) corresponds to a time in which the filaments had already started touching $d_m/\delta \sim 1$. These pictures show that the strain rate is always maximum off the filaments, which agrees with observations by Boratav *et al.* (1992). As collapse is approached, two main maxima regions become dominant, as can be seen in the picture for the overlapping time t_{ov} (figure 13*c*). For this

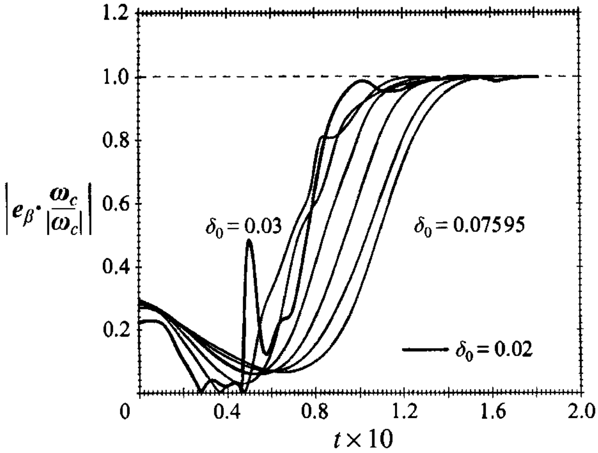

FIGURE 11. Alignment of vorticity ω with the eigenvector e_β of the middle strain-rate eigenvalue, at the collapsing point χ_c, *vs.* time t. The ring parameters are $b = 0.4$, $c = 0.5$ and core radii $\delta_0 = 0.07595$, 0.07, 0.06, 0.05, 0.04, 0.03 and 0.02. The last core radius corresponds to the evolution of the ring in figure 5.

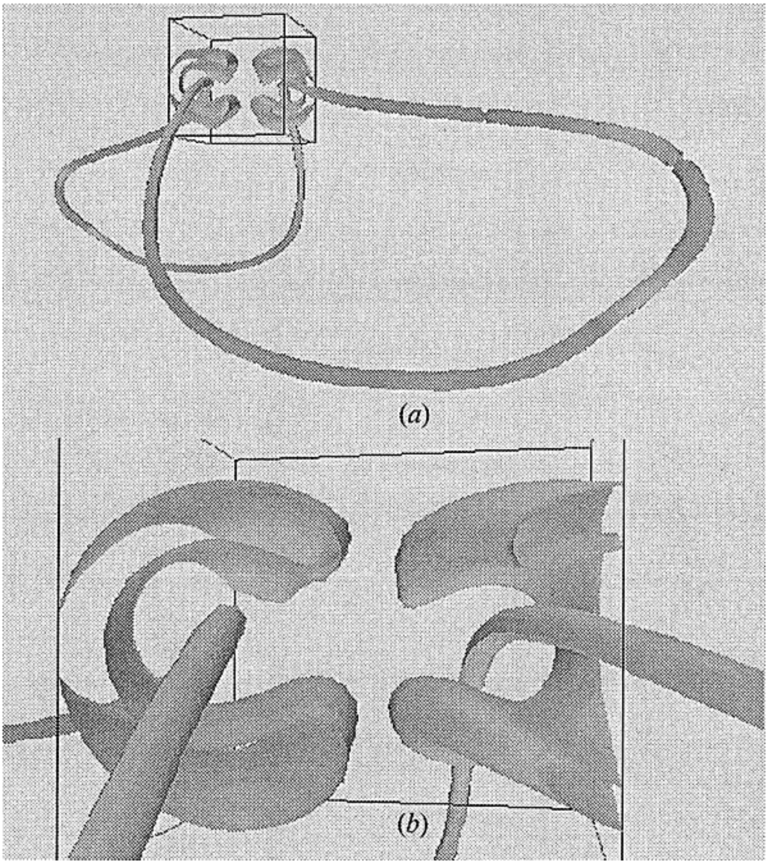

FIGURE 12. (*a*) Diagnostics box for the run with core radius $\delta_0 = 0.07595$ surrounding the collapse region. (*b*) Zoom shows an isosurface of the strain-rate eigenvalue α. The filament thickness shown is one fifth of the actual core radius δ.

last time, representations of the largest positive and largest negative eigenvalues at the upper maximum and on the filament are also shown. The middle eigenvalue, which is positive, perpendicular to the others and aligned with vorticity, has a much smaller relative magnitude and therefore is not visible. For the position of the upper maximum at $t = 0.1806$, we measure a ratio $\alpha/\beta \sim 15$. The eigenvector of α in the upper maximum is horizontal, in the lower maximum is vertical, and on the filament appears rotated about 45° with respect to the previous positions. The orientation corresponding to the entire field can be seen in figure 14. In this figure, we show the eigenvectors of the eigenvalue α in a plane approximately perpendicular to the vortex filaments. We also include the two maxima regions of α in the same plane. The length of the sticks representing the eigenvectors is proportional to α. The pattern of the eigenvectors shown in figure 14 has been observed in continuum simulations of the vortex rings collision by Kida *et al.* (1991). In the case of the second reconnection reported by these authors, the pattern is still present for late times, where reconnection already has an important degree of progression. With respect to the middle eigenvalue, the patterns we observe (not shown) are similar to the ones presented in other experiments and simulations (Schatzle 1987; Winckelmans 1989; Pumir & Siggia 1990; Kerr 1993). The eigenvalue α and its eigenvector were usually not subjects of special attention. Nevertheless, previous descriptions of them (Winckelmans 1989; Kida, Takaoka & Hussain 1991; Kerr 1993) are consistent with what we observe. It seems to be recognized (Jiménez 1992; Kerr 1993) that the eigenvalues α and γ are associated with the two-dimensional nature of the antiparallel configuration of the vortex tubes and that the middle eigenvalue β relates to a three-dimensional effect introduced by the curvature of the vortex tubes.

Particular to our work, we only examined times previous to core overlapping. Also, we measure strain rate off the filament and concentrate our attention on the largest eigenvalue α rather than the middle eigenvalue β, as the first quantity is much larger in magnitude. Previously, attention has been given almost exclusively to β, which aligns with the original filaments. The most important consequence of the characterization of α as given by figures 9, 13 and 14, is that the major impact of any singular or near-singular behaviour of the strain rate and its associated maxima in vorticity amplification does not occur on the original vortex filaments or vortex tubes, but off them, on vorticity aligning with the eigenvector of α. The amplification of this vorticity would be the largest possible in the neighbourhood of the collapse region. In fact we believe that low level or background vorticity picking up this singular or near-singular strain-rate growth, is the mechanism for bridge formation in vortex reconnection.

To compute the normalized vortex stretching (3.22) off the filament, it is necessary to have a distributed vorticity distribution. The filaments defined by (2.3) and (2.4) have non-zero vorticity off the filaments, but it is spurious in the sense that, according to our model, only vorticity on the filament is dynamically relevant. Nevertheless, we wanted to determine whether or not we could establish some kind of comparison of vortex stretching off the filaments with other kinds of simulations by using this spurious, off the filament vorticity distribution. Very close to collapse, the normalized vorticity distribution shows an X-shaped structure, also observed in continuum simulations (Zabusky, Silver & Pelz 1993; also personal communication, T. Scheidegger). At the overlapping time $t_{ov} = 0.1814$ we show in figure 15, in addition to the filaments and eigenvectors, the normalized rate of change of the magnitude of vorticity s_{ω} (see equation (3.23)) represented by the objects, and a vector line, released from one of the objects, that traces the normalized vortex stretching field (3.22). The vortex stretching

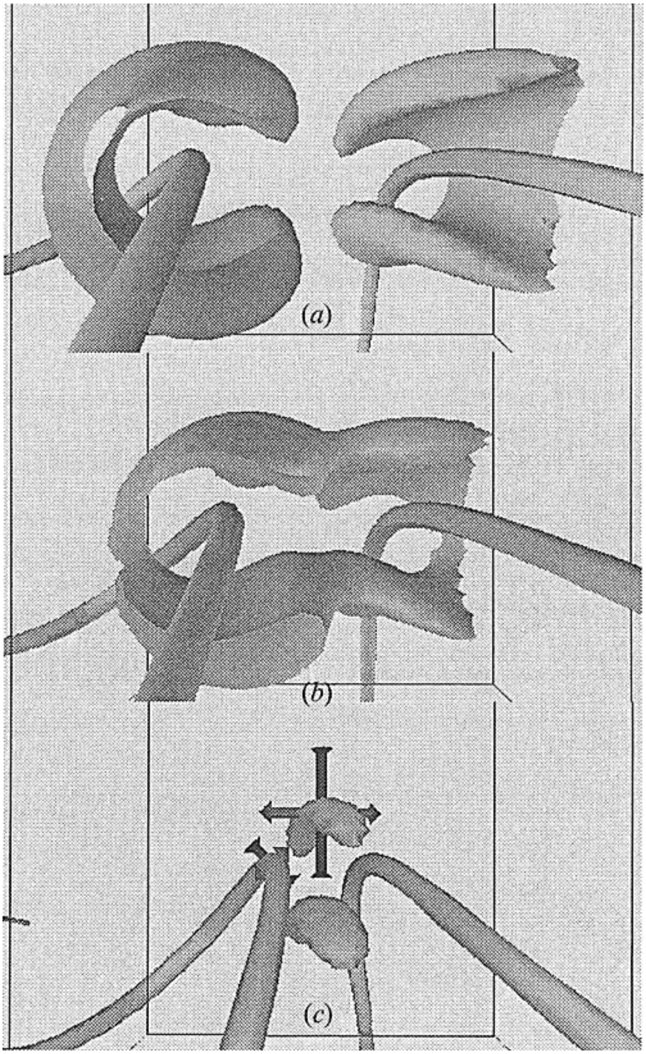

FIGURE 13. Isosurface of the strain-rate eigenvalue α at the times (*a*) $t = 0.18$, (*b*) $t = 0.1807$ and (*c*) $t = 0.1814$ of the evolution of the ring in figure 5. The isosurface threshold is 80% of the maximum at each time shown. Normal arrows represent eigenvectors of α. Arrows with the arrowhead reversed represent eigenvectors of the eigenvalue γ. The filament thickness shown is one fifth of the actual core radius δ.

line shows a 'torus'-like pattern similar to the one observed in continuum simulations of vortex reconnection by Zabusky *et al.* (1991).

6. Collapse energy density

We have at present no theory to explain collapse as established in terms of the parameters in figure 1, which was computed numerically. This section describes initial work we have done to find such a theory. It is important to realize that the variation of geometric parameters and initial core radius of our initial conditions (2.9) corresponds to a variation of the motion invariants. In particular, changing the core radius, while keeping constant the geometric parameters, still represents a

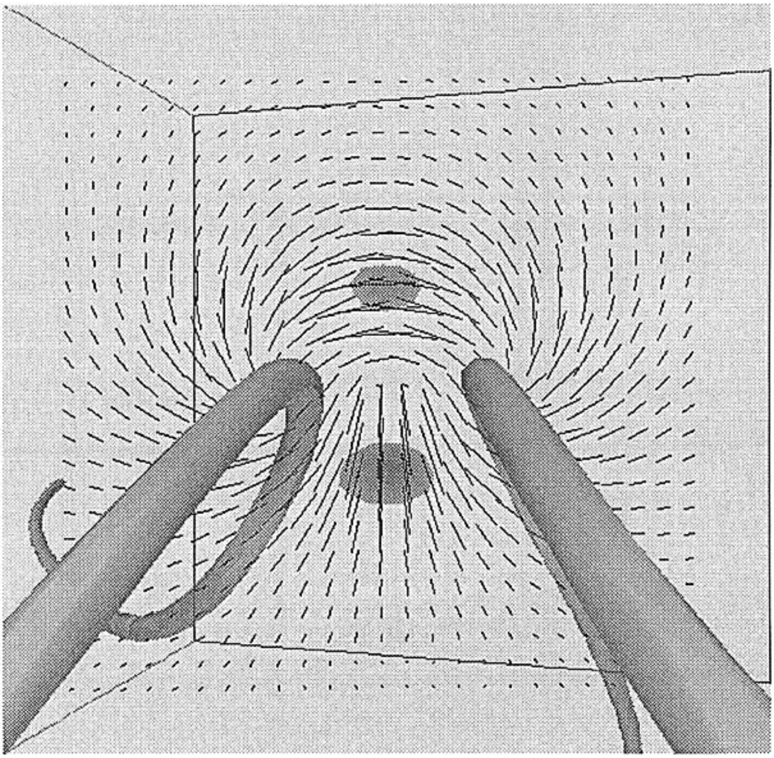

FIGURE 14. Orientation of the eigenvector of the strain-rate eigenvalue α, in the collapse region, at the time $t = 0.1814$ of the evolution ring in figure 5. The upper and lower α maxima are also indicated. The filament thickness shown is one fifth of the actual core radius δ.

change in the total energy of the vortex ring. The graph with the collapse boundary in the parameter space (figure 1), shows the dependence of collapse on the motion invariants.

6.1. *Self-similarity ansatz and zero-energy-density condition*

Previous work has underlined the importance of self-similarity for collapse (Fukuyu & Arai 1991; Pumir & Siggia 1990; Kerr 1993; de Waele & Aarts 1994). We explore the implications of a self-similarity ansatz for the energy of a collapsing configuration. To characterize the state of collapse, we use the following ansatz:

$$\chi(\sigma, t^*) = \lambda(t^*)\ \chi(\sigma, 0) = \lambda(t^*)\ \chi_0(\sigma), \tag{6.1}$$

which can be valid for a whole vortex filament or for some of its regions only.

The energy of a filament is

$$E = \frac{\Gamma^2}{8\pi} \int_{C'} \int_{C} \frac{\mathrm{d}\chi \cdot \mathrm{d}\chi'}{|\chi - \chi'|}\,. \tag{6.2}$$

This expression should be evaluated using a cut off to avoid the singularity in the kernel. Substituting (6.1) in the energy expression, we obtain

$$E = \lambda(t^*)\, \frac{\Gamma^2}{8\pi} \int_{C'} \int_{C} \frac{\mathrm{d}\chi_0 \cdot \mathrm{d}\chi_0'}{|\chi_0 - \chi_0'|} = \lambda(t^*)\, E_0\,, \tag{6.3}$$

which is constant for inviscid motion. The only condition in which the above

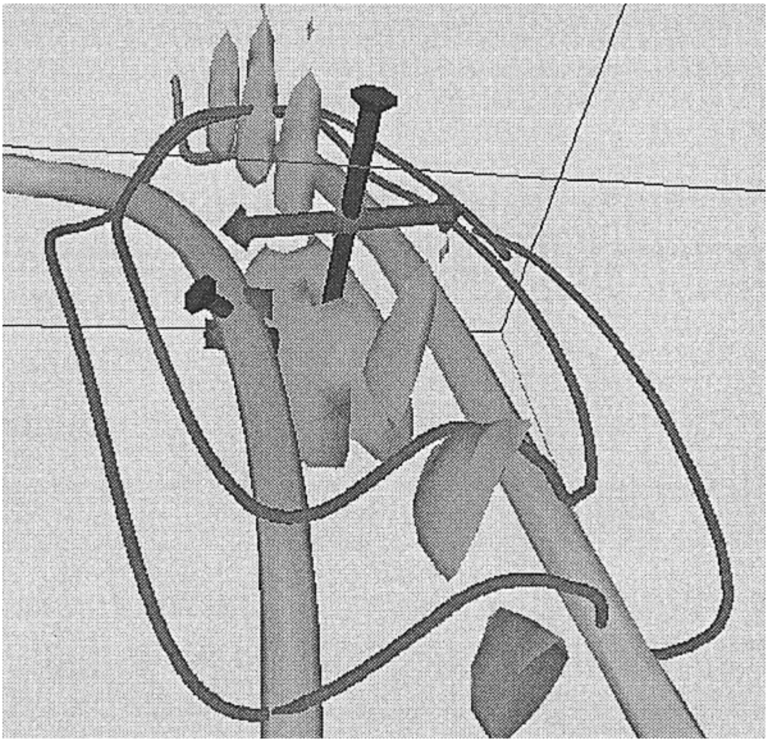

FIGURE 15. Strain rate and vortex stretching fields at $t = 0.1814$ of the evolution of the ring in figure 5. The objects are the isosurface of the normalized rate of change of vorticity s_ω, at 65% of the maximum. The line with the torus-like pattern, launched from one of the vortex stretching objects, traces the normalized vortex stretching field (3.22). The vortex filaments and the eigenvectors of the strain-rate eigenvalues, α and γ, on and off the filament, are also shown at the position of α_m and at the point χ_{d_m}. The filament thickness shown is one fifth of the actual core radius δ.

is true is

$$E_0 = 0 . \tag{6.4}$$

As this condition may apply only locally to the collapse region on the filament, we heuristically choose as diagnostic the energy density

$$\mathscr{E}(s') = \int_C K_{\mathscr{E}}(s', s)\, \mathrm{d}s , \tag{6.5}$$

which is the first integral in the expression for the approximate energy (3.10), with

$$K_{\mathscr{E}}(s', s) = \frac{\mathrm{d}\chi}{\mathrm{d}s'} \cdot \frac{\mathrm{d}\chi}{\mathrm{d}s}\, \psi(|\chi(s) - \chi(s')|) . \tag{6.6}$$

A ‘strong’ condition to have collapse, or $\mathscr{E} = 0$, would be

$$\frac{\mathrm{d}\chi}{\mathrm{d}s'} \cdot \frac{\mathrm{d}\chi}{\mathrm{d}s} = 0 \tag{6.7}$$

along the filament. The ‘weak’ case is when the kernel $K_{\mathscr{E}}$ has mutually cancelling contributions. To verify whether either of these two cases occurs during collapse, we compute the kernel of the energy density $K_{\mathscr{E}}$, defined by (6.6). Analogous substitution of the self-similarity ansatz in the linear and angular impulse definitions results in the collapse conditions $\boldsymbol{P}_0 = \mathbf{o}$ and $\boldsymbol{M}_0 = \mathbf{o}$ also. The linear momentum in the x_3-direction in fact means that the area between the projections onto the plane (x_1, x_2) of the collapsing regions of the filament goes to zero, which in fact is the case. We compute, therefore, the linear and angular impulse density components in the x_3-direction, $\mathrm{d}P/\mathrm{d}s$ and $\mathrm{d}M/\mathrm{d}s$, which are given by the kernels in (3.4) and (3.5). It should be mentioned that Fukuyu & Arai (1991) find with a simple phenomenological model, in the limit $1/\kappa >> d_m >> \delta$, that the contribution of a singular point to the energy tends to zero for self-similar collapse.

6.2. *Calculation of the function λ*

The function λ can be calculated from the velocity on the filament, as given by the Biot-Savart law

$$\dot{\boldsymbol{\chi}} = \dot{\lambda}\,\boldsymbol{\chi}_0 = -\frac{1}{\lambda}\frac{\Gamma}{4\pi}\int_C \frac{(\boldsymbol{\chi}_0 - \boldsymbol{\chi}_0{}') \times \mathrm{d}\boldsymbol{\chi}_0{}'}{|\boldsymbol{\chi}_0 - \boldsymbol{\chi}_0{}'|^3} = \frac{\boldsymbol{u}_0(\sigma)}{\lambda}. \tag{6.8}$$

Taking the dot product with $\boldsymbol{\chi}_0$ we obtain an ordinary differential equation for λ:

$$\dot{\lambda}\,\lambda = \frac{\boldsymbol{\chi}_0 \cdot \boldsymbol{u}_0}{\boldsymbol{\chi}_0 \cdot \boldsymbol{\chi}_0} = -\frac{1}{2t_c^*}, \tag{6.9}$$

with the solution

$$\lambda(t^*) = \left(1 - \frac{t^*}{t_c^*}\right)^{1/2}, \tag{6.10}$$

which agrees with the work by Siggia and Pumir (Siggia 1985; Pumir & Siggia 1987) and was also found by de Waele & Aarts (1994). The strain rate induced by the filament on itself is

$$\frac{(\nabla + \nabla^T)}{2}\boldsymbol{u}(\boldsymbol{\chi}, t^*) = \frac{3\Gamma}{8\pi}\int_C \frac{\mathrm{D}(\boldsymbol{\chi} - \boldsymbol{\chi}')\,\mathrm{d}\boldsymbol{\chi}'}{|\boldsymbol{\chi} - \boldsymbol{\chi}'|^5}, \tag{6.11}$$

which has to be evaluated with a cut off. The operator D is defined in equation (3.17). After substituting the self-similarity ansatz (6.1) in the previous expression, we find the self-similar form

$$\frac{(\nabla + \nabla^T)}{2}\boldsymbol{u}(\boldsymbol{\chi}, t^*) = \frac{1}{\lambda^2}\frac{(\nabla + \nabla^T)}{2}\boldsymbol{u}_0 = \frac{t_c^*}{t_c^* - t^*}\frac{(\nabla + \nabla^T)}{2}\boldsymbol{u}_0, \tag{6.12}$$

which is singular for $t_c^* > 0$.

6.3. *Global and local diagnostics with the energy density*

In figure 16, we present the computed evolution in time at the collapsing point $\boldsymbol{\chi}_c$ of the linear and angular impulse density components in the x_3-direction, $\mathrm{d}P_c/\mathrm{d}s$ and $\mathrm{d}M_c/\mathrm{d}s$, the energy density $\mathscr{E}_c$ and the energy density kernel $K_{\mathscr{E}c}$. The energy density kernel $K_{\mathscr{E}c}$ is computed with both s and s' corresponding to $\boldsymbol{\chi}_c$. Therefore, it represents the local contribution to the energy density at the collapsing point. All of these graphs correspond to the bounce case in figure 5, with the strain rate in figure 9. The bounce is visible in the graphs of linear impulse $\mathrm{d}P_c/\mathrm{d}s$ (figure 16*a*), and energy density $\mathscr{E}_c$ (figure 16*b*), as a valley at about $t = 0.11$, followed by a rapid decay as collapse takes place. The angular impulse density $\mathrm{d}M_c/\mathrm{d}s$ also decays (figure 16*a*), but does not show the bounce present in the other graphs. The kernel of the energy density at the collapsing point $K_{\mathscr{E}c}$ has faster than exponential growth, as can be seen qualitatively in the semi-logarithmic graph in figure 16(*a*), even though the energy

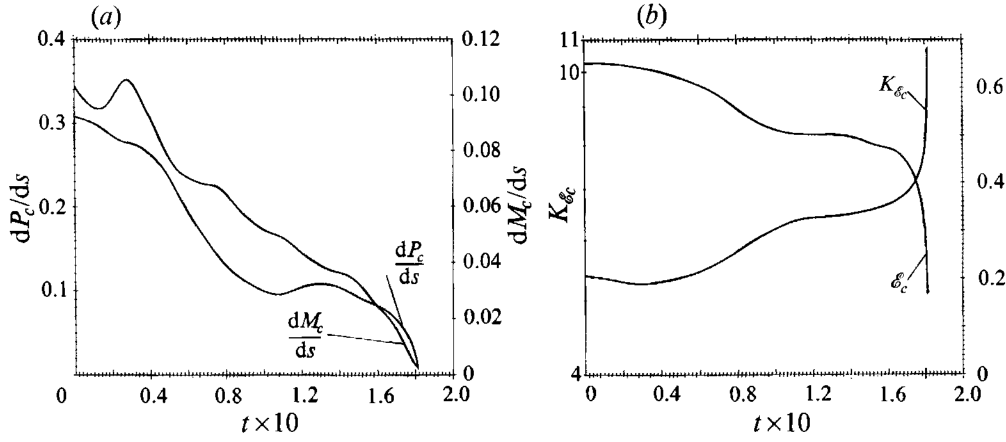

FIGURE 16. Evolution of (*a*) linear and angular impulse densities, $\mathrm{d}P_c/\mathrm{d}s$ and $\mathrm{d}M_c/\mathrm{d}s$; and (*b*) energy density kernel $K_{\mathscr{E}c}$ and energy density $\mathscr{E}_c$ at the collapsing point χ_c. The parameters of the ring correspond to figure 5.

density $\mathscr{E}_c$ is approaching zero at the same time. The rapid decay in the linear impulse, angular impulse and energy densities is in agreement with the conditions suggested by the self-similarity ansatz and therefore constitutes signatures of collapse.

To obtain a more complete picture of collapse, we examine in detail diagnostics along the vortex ring for $t = 0.18$, which is close to the collapse time, but still before the validity limit is reached. In the following graphs, the origin is at the value of s corresponding to the point χ_{d_m} which, by this time, is very close to the collapsing point χ_c (see figure 5). In figure 17, for the same time as the previous graphs, we show the linear and angular impulse density components, $\mathrm{d}P/\mathrm{d}s$ and $\mathrm{d}M/\mathrm{d}s$, the kernel of the energy density $K_{\mathscr{E}}$, with s' corresponding to the point χ_{d_m}, and the energy density $\mathscr{E}$ *vs.* arc length s. The linear impulse density $\mathrm{d}P/\mathrm{d}s$ has regions close to zero surrounding the collapsing segments of the ring. The angular impulse density $\mathrm{d}M/\mathrm{d}s$ shows a zero very close to the collapsing point, but we had expected a wider region close to zero. We observe that the kernel of the energy density $K_{\mathscr{E}}$ presents two opposite, cancelling contributions, one local and the other mutually inductive. This shows that collapse corresponds to the 'weak' case referred to before. The plot of the energy density $\mathscr{E}$ shows that the collapsing regions on the ring correspond to very localized minima, approaching zero as time increases.

6.4. *Energy density as a criterion for surgery*

A scenario of the change in the contributions to the energy in a collapsing vortex tube has been proposed by Chorin (1990*a*), but the considerations presented there are for local collapse and therefore are not relevant to the antiparallel configuration formation of our non-local collapse case in § 5. In his scenario of local collapse, Chorin maintains that the self-energy, or the contribution to the energy due to local interactions or interactions of vortex segments with themselves, increases as the filament stretches. In order to maintain constant energy, the mutual contributions must become negative, which means the tube should fold. In terms of the energy density $\mathscr{E}$, the picture we observe for non-local collapse is as follows. Even though the local contribution $K_{\mathscr{E}c}$ to the energy density $\mathscr{E}$ increases, as the larger peaks in the $K_{\mathscr{E}c}$ and $K_{\mathscr{E}}$ plots in figures 16 and 17 show, these increases are cancelled by the

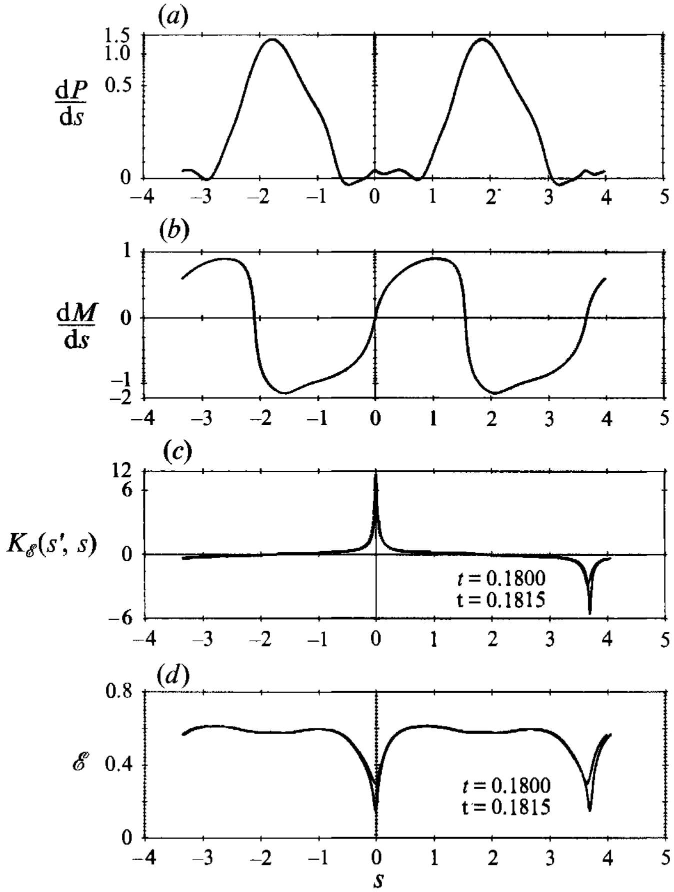

FIGURE 17. (*a*) Linear impulse density $\mathrm{d}P/\mathrm{d}s$, (*b*) angular impulse density $\mathrm{d}M/\mathrm{d}s$ (*c*) energy density kernel $K_{\mathscr{E}}$ and (*d*) energy density $\mathscr{E}$ *vs.* arc length s, at the time $t = 0.18$ of the evolution of the ring in figure 5. In (*b, c*) the last two graphs the curves for $t = 0.1815$ are also included. The origin $s = 0$ in the plots and s' in the energy density kernel computation correspond to the point χ_{d_m}.

other approaching antiparallel segment of the filament, not maintaining the energy density constant, but reducing it to zero through the cancellation (figure 17).

In three-dimensional vortex methods, collapse results in paired antiparallel filaments, which have a minimal contribution to the kinetic energy of the flow, as the results in the previous paragraph indicate. The paired filaments consume excessive computational resources, making the continuation of the computations practically impossible. This necessitates a surgery algorithm to eliminate these collapsed filament segments. Such an algorithm has been proposed by Chorin (1990*b*, 1993). In this algorithm, regions undergoing non-local collapse are identified using criteria of closeness of approach and orientation. Surgery is performed assuming these regions have 'infinite temperature'. In contrast with the condition of infinite temperature for collapse, the zero-energy-density criterion we are suggesting can be quantified in a straightforward manner. Therefore, we believe that the energy density could be used as a diagnostic quantity for a surgery algorithm. Also, the surgery of zero- or low-energy-density segments of the filaments only constitutes a small change in the total energy of the flow, which means an algorithm with very small dissipation.

7. Multi-filament simulations

The objective of performing multi-filament simulations is to observe the behaviour of the collapsing LE vortex ring as new degrees of freedom are introduced. The two aspects we will examine are, first, whether or not the formation of smaller scales, allowed by the multi-filament model, destroys the evolution towards collapse and, second, the characteristics of vorticity and strain-rate amplification during the close vortex interaction. We find that the $O(n^2)$ nature of the Biot-Savart direct method (where n is the number of grid points in the ring) severely limits the multi-filament collapse computation. Previous simulations with direct methods include the stability study of a vortex ring by Knio & Ghoniem (1990) with a maximum of 7320 grid points, the vortex ring collision problem (vortex ring merger) by Anderson & Greengard (1989) with a maximum of 5490 grid points per ring, the same case by Winckelmans (1989) with a maximum of 6272 grid points per ring and the simulation of a circular ring with different initial perturbations by Inoue (1988) with a maximum of 1180 grid points. From the single-filament runs, we know that in order to observe a large vorticity amplification, we need a small ring thickness δ_C, but, to have a small core size, it is necessary to increase the number of grid points in order to keep the overlapping (resolution) to an acceptable minimum. Therefore there is a trade-off between the ring thickness and the number of grid points we can use. The parameters of the ring we select are a compromise between ring thickness and computational expense. Notice that the case $\delta_C = 0.07595$, which we present later in detail, corresponds to the lowest strain-rate amplification in our single-filament studies. Our simulations have a relative large ring thickness δ_C, even though we initially employed up to 45720 grid points. We exploit the antisymmetry of the ring, so that the velocity has to be computed only at half the grid points. The more interesting cases with higher vorticity amplification, observed in the previous single-filament simulations, will require the use of fast summation techniques.

7.1. *Multi-filament Biot-Savart model*

The multi-filament algorithm is obtained by extending the expressions for the single-filament ring. The vorticity of the multi-filament ring is (2.3)

$$\omega(x,t^*) = \sum_{i=1}^{n_f} \Gamma_i \int_C \mathrm{d}\chi_i(\sigma,t^*)\, f_\delta(|x-\chi_i(\sigma,t^*)|)\,, \tag{7.1}$$

which is the sum of the contributions of each filament forming the vortex tube. The total number of filaments in the ring is n_f.

The velocity induced by the multi-filament ring is now (2.5):

$$u(x,t^*) = -\frac{1}{4\pi}\sum_{i=1}^{n_f} \Gamma_i \int_C \frac{(x-\chi_i)\times \mathrm{d}\chi_i}{|x-\chi_i|^3}\, g(|x-\chi_i|)\,. \tag{7.2}$$

The function g is defined by (2.6).

The strain rate is (3.18)

$$\frac{(\nabla+\nabla^T)}{2}u(x,t^*) = \frac{1}{8\pi}\sum_{i=1}^{n_f} \Gamma_i \int_C \varphi(|x-\chi_i|)\,\mathrm{D}(x-\chi_i)\,\mathrm{d}\chi_i\,, \tag{7.3}$$

where $\varphi(\rho)$ is defined by (3.20) and D by (3.17). Using this equation, we compute, as diagnostics, the strain-rate eigenvalues, the normalized vortex stretching (3.22), and the normalized rate of change of the magnitude of vorticity (3.23) for the multi-filament ring. We also compute the distance d_m (3.25), introduced earlier. For the multi-filament ring we find the minimum distance d_m for all the filaments, and for the grid points on the centreline.

7.2. *Vortex ring discretization*

The multi-filament LE ring is constructed around either the centreline given by (2.9) or the centreline corresponding to the position of a single-filament ring at some time close to the collapse time. Once the n_0 grid points in the centreline are established, construction of the multi-filament ring proceeds by distributing the filaments concentrically in n_l 'layers' around the centreline. At each grid point in the centreline, using a cubic spline, we compute the local Frenet–Serret coordinate system, i.e. the unit tangent $\hat{\boldsymbol{t}}$, normal $\hat{\boldsymbol{n}}$, and binormal $\hat{\boldsymbol{b}}$ vectors (3.3). The grid points on the concentric n_l filament layers are distributed on planes normal to the centreline, defined by the local coordinate system. Each concentric filament layer is located at a radius

$$r = k\,\frac{\delta_C}{n_l} \tag{7.4}$$

and has

$$n_a \;=\; 6k \tag{7.5}$$

filaments, where k is the layer number (for the first layer $k = 1$, for the outer layer $k = n_l$, the centreline is $k = 0$) and δ_C is the thickness of the multi-filament ring (figure 18). Every time a new layer of filaments is produced, this layer is shifted in the azimuthal direction by $2\pi/n_a$ rad to avoid alignment of filaments in the radial direction. The distances between filaments in the radial and azimuthal directions are (figure 18)

$$h_r \;=\; \frac{\delta_C}{n_l} \quad\text{and}\quad h_a \;=\; \frac{2\pi h_r k}{n_a}\,. \tag{7.6}$$

In the cross-section of the ring, for a distribution of filaments given by (7.4) and (7.5), the overlappings in the radial and azimuthal directions are

$$q_r \;=\; \frac{2\delta_0}{h_r} \;=\; 2\,\frac{\delta_0}{\delta_C}\,n_l \quad\text{and}\quad q_a \;=\; \frac{2\delta_0}{h_a} \;=\; \frac{6}{\pi}\,\frac{\delta_0}{\delta_C}\,n_l\,, \tag{7.7}$$

where δ_0 is the initial filament core size at each grid point. For $\delta_C/\delta_0 \sim 2$ and $n_l = 4$, q_r and $q_a \sim 4$.

The circulation of each filament is assigned according to $\Gamma_i = C_e \exp(\,-r_i^3/\delta_C^3\,)$, where r is the distance from the ith filament to the centreline of the ring (7.4). The normalization constant C_e is chosen, so that the total circulation is $\Gamma_C = \sum_{i=0}^{n_f} \Gamma_i = 1$, where the total number of filaments distributed in the n_l concentric layers (7.5) and the centreline of the ring is $n_f = 1 + 3n_l(n_l + 1)$. Each concentric layer has n_a filaments (7.5) (see figure 18). The total initial number of grid points is $n_{t0} = n_0\, n_f$, where n_0 is the initial number of grid points per filament.

The time step was chosen based on the experience with the single-filament runs and the following estimate. We define a maximum time step

$$\Delta t^{*} \;<\; \frac{\Delta x_c}{u_c}\,. \tag{7.8}$$

The critical velocity u_c is the velocity magnitude at the core δ_0 of a rectilinear,

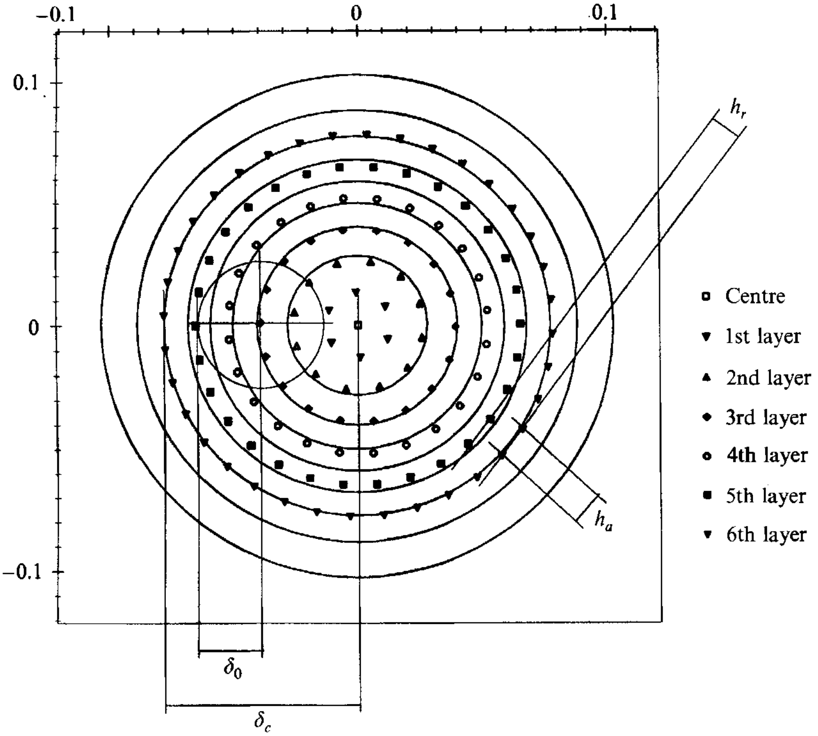

FIGURE 18. Cross-section of the initial condition for a ring with $\delta_C = 0.07595$ and $\delta_0 = 0.05$. The number of layers is $n_l = 6$ and the number of filaments is $n_f = 127$. The contours are vorticity magnitude from 0 to 100% of the maximum.

infinite, or two-dimensional point vortex and the critical grid distance Δx_c is the radial inter-filament spacing

$$u_c = \frac{\Gamma_i}{2\pi\delta_0} \quad \text{and} \quad \Delta x_c = h_r = \frac{\delta_C}{n_l}. \tag{7.9}$$

Using the normalization $t = t^*/t_s = t^* \Gamma_C/(4\pi a^2)$ (2.15), the maximum time step is

$$\Delta t < \frac{1}{2a^2}\frac{\delta_0 \delta_C}{n_l} < \frac{1}{2a^2}\frac{\Gamma_C}{\Gamma_i}\frac{\delta_0 \delta_C}{n_l}, \tag{7.10}$$

where the quantity in the centre is a lower bound (notice that $\Gamma_C/\Gamma_i > 1$) that is used as a conservative rule. The geometric parameter $a = 1$ in our initial condition (2.9).

We performed simulations with the constant- and variable-core models (Fernandez 1994). The main feature of the constant-core simulations is the nearly constant vorticity and the saturation of strain-rate amplification. However, it must be noticed that for this model, the conservation of volume is violated in the regions of large filament stretching, which are present during the close vortex interaction.

7.3. *Variable-core simulations*

To lower the expense of the higher-resolution runs with the variable-core model, we started the multi-filament computations from an initial condition corresponding to the evolution of a single-filament ring at a time close to collapse. The parameters of the runs are presented in table 1. From two series of runs with $\delta_C = 0.1$ and 0.07595, only the latter is presented. The single-filament ring at $t = 0.135$, when

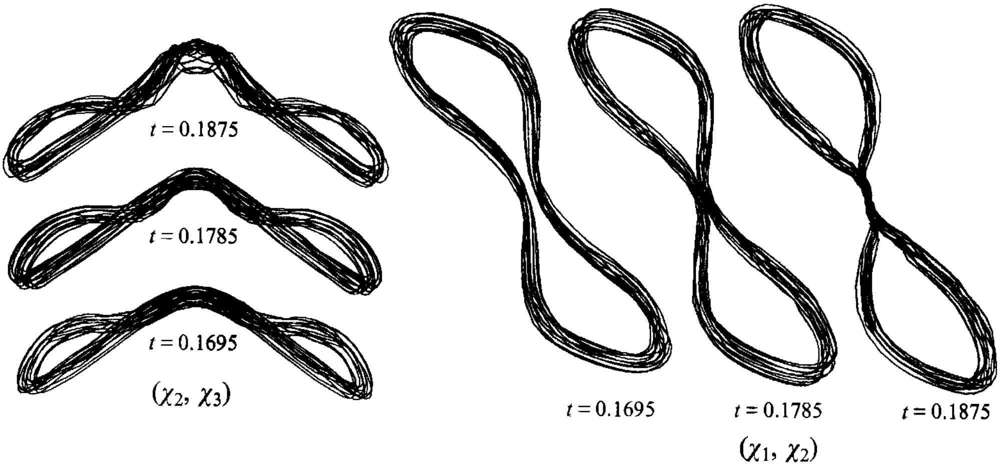

FIGURE 19. Evolution of the variable-core multi-filament ring v6. The single-filament ring had initially $a = 1, b = 0.4, c = 0.5, \delta_C = 0.07595$ and $\Gamma_C = 1$. The multi-filament ring has $n_l = 6$ layers, $n_f = 127$ filaments and $n_0 = 360$ grid points per filament for a total of $n_{t0} = 45\,720$ grid points initially. The times in the evolution are $t = 0.1695, 0.1785$ and 0.1875. Only every 10th filament and only every 6th grid point are displayed. Position of projections does not correspond to actual motion of the ring.

Run	δ_0	n_l	n_f	n_0	n_{t0}
v1	0.07595	0	1	360	360
v2	0.04	4	61	360	21 960
v3	0.04	5	91	360	32 760
v4	0.04	6	127	360	45 720
v5	0.05	5	91	360	32 760
v6	0.05	6	127	360	45 720

TABLE 1. Multi-filament runs with the variable-core model. Multi-filament simulations start from a single-filament ring with $a = 1, b = 0.4, c = 0.5$, $\delta_C = 0.07595$ and $\Gamma_C = 1$ at $t = 0.135$. The time step was $\Delta t = 3 \times 10^{-4}$. Runs v4 and v6 were recomputed with $\Delta t = 1.5 \times 10^{-4}$ in the intervals $0.18 \leqslant t \leqslant 0.1875$ and $0.165 \leqslant t \leqslant 0.192$ respectively.

the inter-filament distance is $2d_m/\delta_C \sim 3.33$, is used as the centreline to generate the multi-filament ring. The outer filament layer is at a distance δ_C from the centreline. According to the conservative rule in (7.10), the time step for $\delta_0 = 0.04$ and $n_l = 5$ should be $\Delta t = 3.038 \times 10^{-4}$. In the single-filament runs with variable core, for $\delta_0 = 0.07595$, the time step $\Delta t = 5 \times 10^{-4}$ shows an accuracy of three significant figures in the average velocity. For the single-filament case with $\delta_0 = 0.04$, the time step we used was $\Delta t = 10^{-4}$, but the circulation of this single-filament ring was $\Gamma = 1$ (in the multi-filament case $\Gamma_C/\Gamma_i > 1$, also see inequality 7.10). The time step selected in these multi-filament variable-core computations was $\Delta t = 3 \times 10^{-4}$. For the higher-resolution cases v4 and v6, we repeated the final portion of the runs with half the time step. The evolution of the ring with the variable-core model for the highest resolution v6 can be seen in figure 19, where only every 10th filament and every 6th grid point on each filament, are displayed. At the end of the variable-core multi-filament runs, including the highest resolution v6, we observe the development of a smaller wavy structure on top of the collapse region, which we present in coming paragraphs.

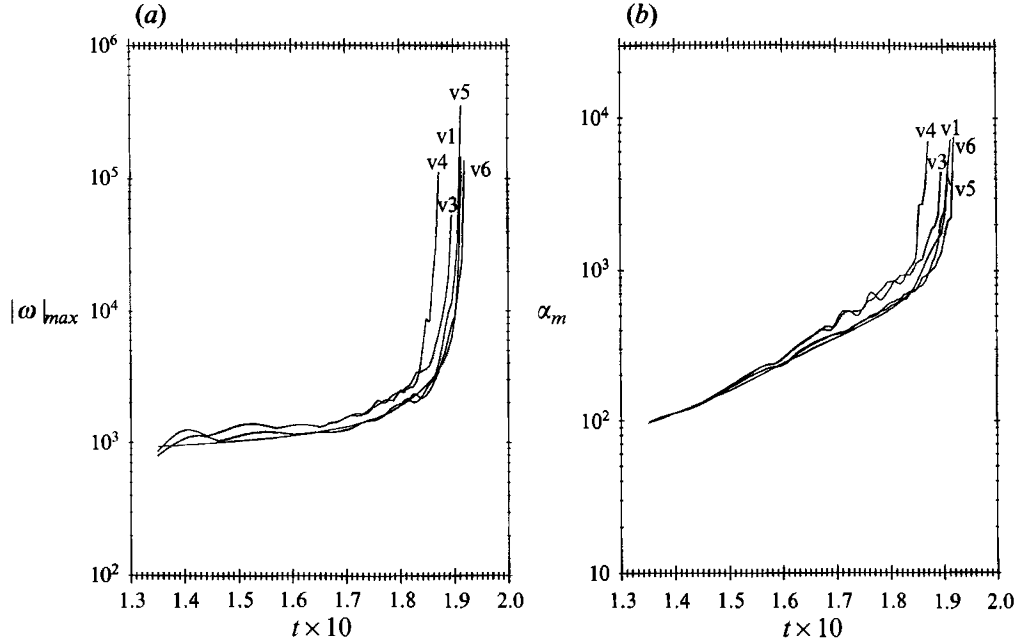

FIGURE 20. Diagnostics for the variable-core model with with $\delta_0 = 0.04$ (v3, v4) and 0.05 (v5, v6). (*a*) Maximum vorticity magnitude $|\omega|_{max}$ on the ring *vs.* time *t*. (*b*) Strain-rate eigenvalue α_m *vs.* time *t*. The cases presented are for runs v1 and v3 to v6 with $n_l = 0$ (single-filament), $n_l = 5$, 6 and $a = 1, b = 0.4, c = 0.5, \delta_C = 0.07595, \Gamma_C = 1$.

In figure 20 we show the resolutions v3, v4, v5 and v6. The two last have larger filament core size $\delta_0 = 0.05$. Run v6 with half the time step did not show significant differences. The smaller filament core size, $\delta_0 = 0.04$, has a somewhat faster vorticity and strain-rate amplification. In general, even though the evolution of the collapse and the characteristics of the collapse region are similar for all of the runs, we do not observe a clear trend towards convergence as we change the resolution. Our results seem to be dependent on the initial filament core size δ_0, which has also been observed in other simulations (Anderson & Greengard 1989; Almgren, Buttke & Colella 1994). We believe the solution of this question will require convergence studies at smaller values of the filament core size δ_0, since the ratio of $\delta_C/\delta_0 \sim 2$ employed in current simulations, including ours, is still far from the condition that δ_0 must be much smaller than any scale in the flow. An important difference with respect to the constant-core simulations is that the maximum vorticity magnitude and the maximum strain rate do not saturate, but continue to grow during the close vortex interaction. The largest growth starts with the appearance of the smaller vortex structure on the top of the collapse region. Even though this vortex structure appears consistently for all resolutions examined, further convergence testing at lower values of δ_0 is required.

We now examine more closely the case with the higher resolution v6. The evolution towards collapse is shown in figure 19 for the times $t = 0.1695, 0.1785$ and 0.1875. This ring initially had $n_{t0} = 45720$ grid points, which by the end of the run increased to $n_t = 189906$ (this last time not shown). The particular feature of the evolution of the ring is the small inverted S-shaped wave forming in the upper part of the collapse region. In figure 21 we present cross-sections of the ring showing vorticity contours (left portion) and the position of the filaments in the time $0.165 < t < 0.1875$. The

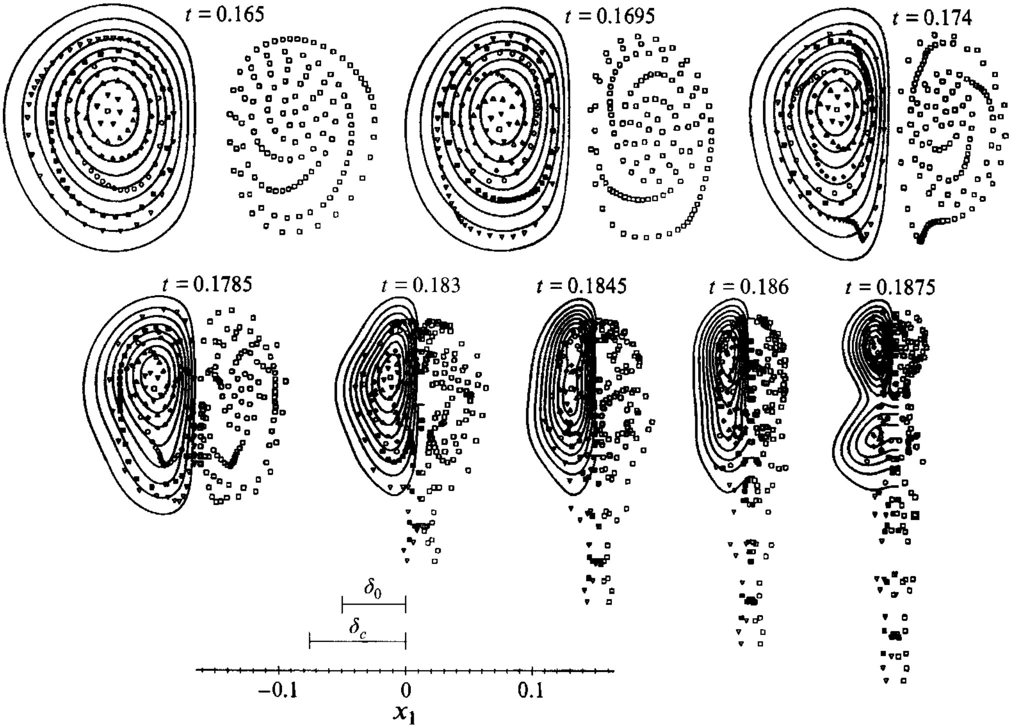

FIGURE 21. Vorticity cross-sections (left half) and distribution of vortex filaments at $t = 0.165$, 0.1695, 0.174, 0.1785, 0.183, 0.1845, 0.186 and 0.1875, for the resolution $n_l = 6$, with filament core radius $\delta_0 = 0.05$ (run v6). The last four times are at shorter intervals. The thresholds of the vorticity contours are between 0 and 100% of the maximum. In the left portion of the dipole the filament layers are coded using different symbols (see figure 18).

intervals between the last four time frames in the figure are shorter. The cross-sections are located at the point of closest approach χ_{d_m} (3.25) and are normal to the vorticity at that point. The filament layers are marked with different symbols (left portion of the cross-sections). The open square marks the centre of the filament. The thresholds of the vorticity magnitude contours are between 0 and 100% of the maximum. We observe the core flattening process characteristic of the close vortex interaction, which has been observed in previous continuum (Ashurst & Meiron 1987; Pumir & Kerr 1987; Pumir & Siggia 1990; Shelley & Meiron 1991; Kida *et al.* 1991; Zabusky *et al.* 1991; Boratav *et al.* 1992) and Lagrangian (Anderson & Greengard 1989; Winckelmans 1989) simulations. The smaller, upper dipole structure at the last time shown, $t = 0.1875$, corresponds to the formation of the S-shaped structure.

In figure 22, we attempt to quantify the dipole structure in the cross-sections presented. These quantifications consist of histograms produced by averaging the core size of the filaments and their circulation in horizontal bins or bands with width Δx_3 (in the vertical direction) and length covering one half of the cross-section of the dipole in the horizontal direction x_1 (see figure 21). The histograms on the left of figure 22 show the distribution of the core size with respect to the vertical x_3-axis. The points correspond to a scatter plot in which the vertical axis is the actual value of the filament core size δ. The continuous line is the average core size in each bin. The second set of histograms (plots on the right in figure 22) present the same type of information, but now the points indicate the circulation Γ_i of each filament. The

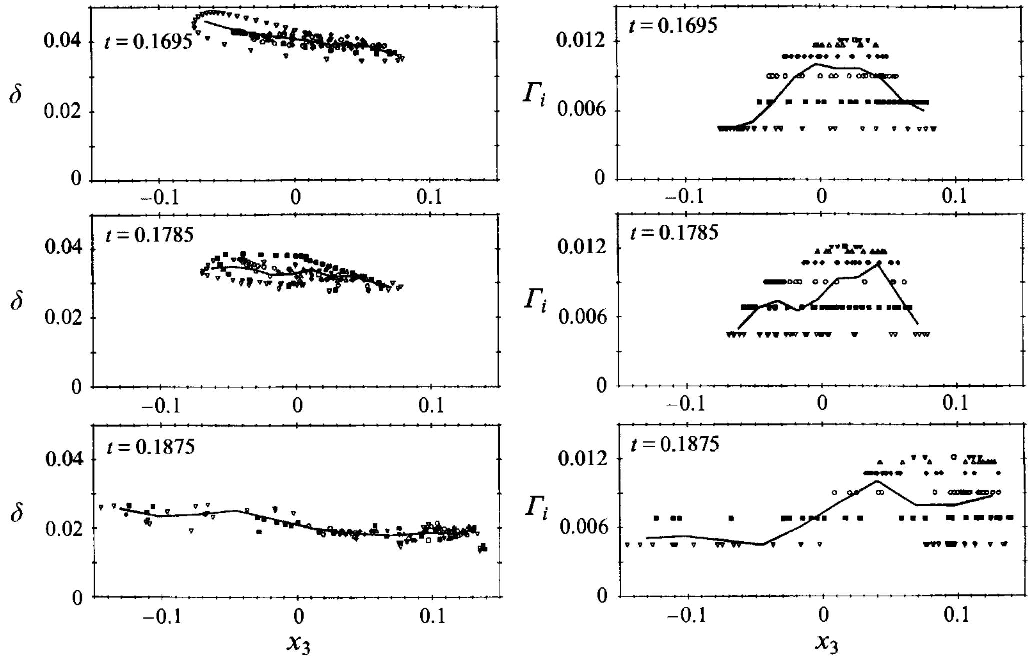

FIGURE 22. Scatter plots with the distribution of the filament core radii δ (left) and filament circulation Γ_i (right) in the vertical x_3-direction (see figure 21). The continuous lines are the average filament core radius and the average filament circulation respectively. The times are $t = 0.1695, 0.1785$ and 0.1875, for run v6. The points are coded according to the filament layers (see figure 18).

continuous line is the average circulation in each bin. The codes of the points can be seen in figure 18. The number of bins is kept constant for all of the times shown, but their width Δx_3 changes as the elongation of the dipole structure in the cross-section increases (the bins cover from the minimum x_3 coordinate of the filaments to the maximum at each time). The times shown are $t = 0.1695, 0.1785$ and 0.1875. The histograms with the filament core size distribution indicate how the core size decreases with time. The smaller core sizes tend to concentrate in the upper part of the dipole, where the vorticity maximum is. The circulation histograms show that the upper part of the filaments always have the larger proportion of the circulation.

The evolution of the vorticity for run v6 ($\delta_0 = 0.05$, $n_l = 6$) is shown in the diagnostics box surrounding the collapse region, in figure 23. The isosurface of the vorticity magnitude, shown in this figure, is at the threshold 40% of the maximum for the times $t = 0.183, 0.1845, 0.186$ and 0.1875. The view shown is at 45° rotation from the top view, or plane (χ_1, χ_2). In this sequence we observe the S-shaped structure formed by the upper filaments. For this filament core size, $\delta_0 = 0.05$, this upper structure is thicker than in the case $\delta_0 = 0.04$, which we show in figure 24. This upper structure has the vorticity maximum at the last time shown $t = 0.1875$ in figure 23 (also see figure 21).

In figure 24 we observe the evolution of the vorticity for run v4 ($\delta_0 = 0.04$, $n_l = 6$). The isosurface of the vorticity magnitude is at the threshold 40% of the maximum for the times $t = 0.18, 0.1815, 0.1830$ and 0.1845 (the evolution of collapse for this filament core size is faster, see figure 20). In this case, the rotation of the upper filaments as the wavy structure forms produces the finger-like appearance in the

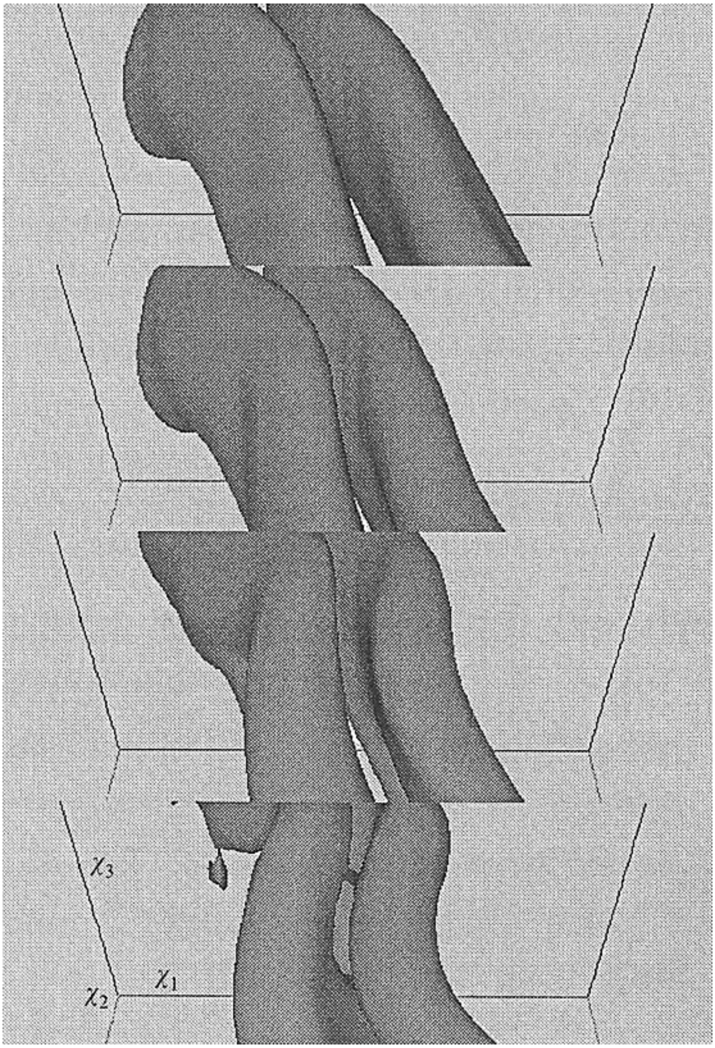

FIGURE 23. View of the collapse region, for the resolution $n_l = 6$, with filament core radius $\delta_0 = 0.05$ (run v6). The vortex tubes are represented by the isosurface of the the vorticity magnitude at the threshold 40% of the maximum. The times are $t = 0.183$ (top), 0.1845, 0.186 and 0.1875 (bottom).

vorticity isosurface. Even though the vorticity has this finger-like shape, the vortex filaments are not folding back on themselves, but continue beyond the tip of the fingers (with lower vorticity of course), completing the 'S'-shape of the upper vortex structure. It is important to notice that, as the upper vortex structure rotates, it tends to align with the direction of the largest strain-rate eigenvalue α which is oriented, in the maximum upper region, perpendicular to the original antiparallel configuration (shown in Fernandez 1994). This upper S-shaped vortex structure, has the maximum vorticity amplification by the last time in figure 24.

The strain-rate eigenvalue fields α and β continue to present the same orientation observed in the single-filament simulations, although the structure of the maxima regions is different. In the case of α, the maximum region corresponds to an inverted U-shape (Fernandez 1994). In figure 25, we observe the top view, or plane (χ_1, χ_2), of the collapse region at the time $t = 0.183$ of run v6. The vortex tubes are represented

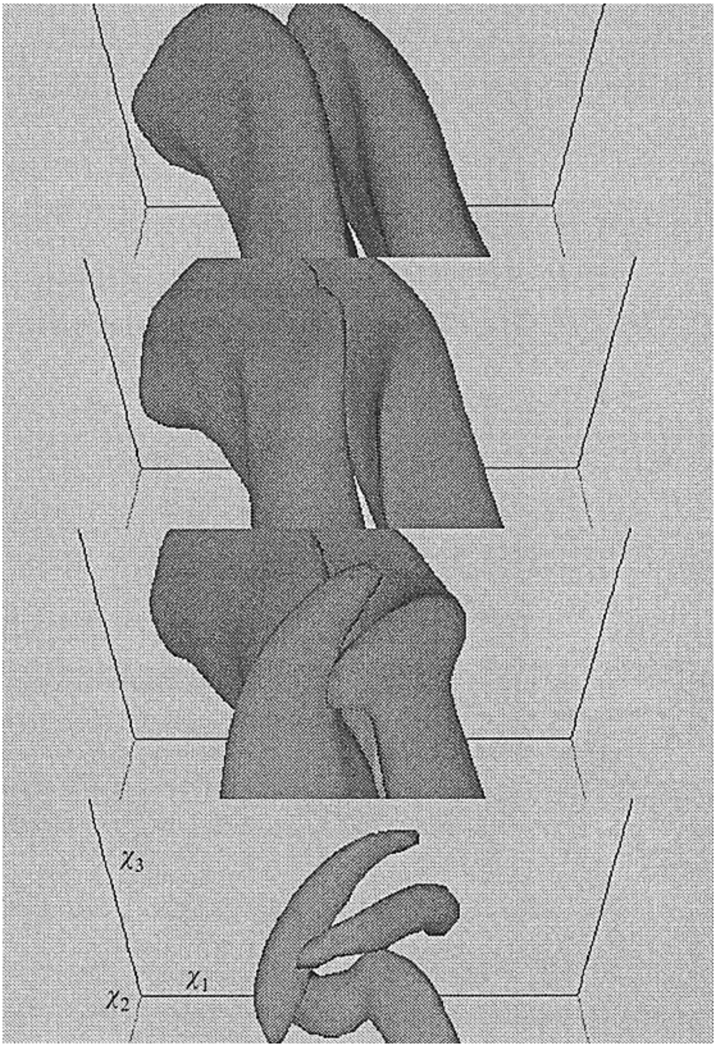

FIGURE 24. View of the collapse region, for the resolution $n_l = 6$, with the filament core radius $\delta_0 = 0.04$ (run v4). The vortex tubes are represented by the isosurface of the the vorticity magnitude at the threshold 40%. The times are $t = 0.18$ (top), 0.1815, 0.183 and 0.1845 (bottom).

by the isosurface of the vorticity magnitude at the threshold 90% of the maximum. The smaller objects in the upper and lower part of the view shown, in between the vortex tubes, are the isosurface of the normalized rate of change of the magnitude of vorticity (3.23) at the threshold 75% of the maximum. The vector lines, released from a plane located in the upper part of the collapse region, trace, with positive and negative integration step, the normalized vortex stretching field (3.22). We observe that we have again a pattern similar to that found in the single-filament simulation. In the other hand, this pattern comes closer to the 'torus' shape observed in the continuum simulations (Zabusky *et al.* 1991).

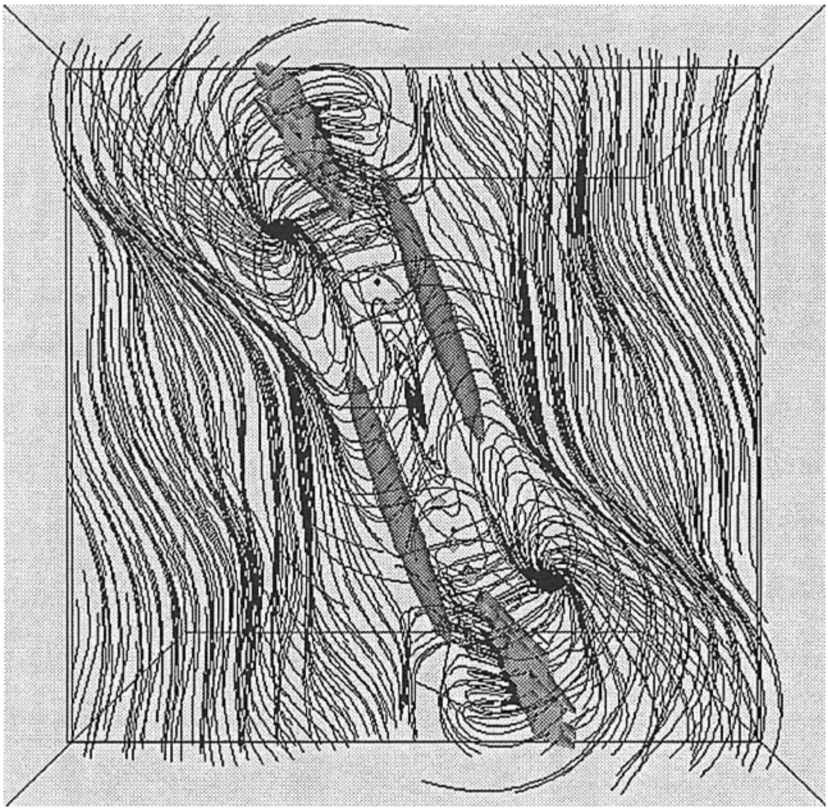

FIGURE 25. Vortex stretching pattern. This top view, or plane (χ_1, χ_2), of the collapsing region shows the isosurface of the vorticity magnitude at the threshold 90% of the maximum, for run v6. The time is $t = 0.183$. The smaller objects between the vortex tubes are the isosurface of the normalized rate of change of the magnitude of vorticity at the threshold 75% of the maximum. The vector lines trace the normalized vortex stretching.

8. Conclusions

The study of a simple collapsing vortex configuration, the Lissajous-elliptic (LE) vortex ring, has been presented. Exploration of the parameter space showed the different types of evolution of this ring and the collapse boundaries for three core radii. The periodic regime of the vortex ring is suitable for examining the long-time behaviour of the Biot-Savart model. We find that the algorithm breaks down through the appearance of a short-wave instability that becomes a 'local' collapse (figure 2). This instability of the single-filament Biot-Savart model is spurious because its wavelength is of the order of the core radius.

In our single-filament simulations we find that the non-local collapse regime of the LE vortex ring exhibits a dependence on the initial core radius. *Non-monotonic collapse* can be induced by choosing a sufficiently small initial core radius. In the parameter space, this behaviour is visible as a shift of the collapse boundary towards higher levels of energy (figure 1). Quantification of the *off the filament* strain rate shows faster than exponential growth prior to core overlapping. By fitting the functional form (5.1), we find that α_m approaches *self-similar, singular-like* behaviour in a small region close to the end of the validity limit of the Biot-Savart model. Plots of the vorticity magnitude on the filament in semi-logarithmic scales also show, qualitatively, faster than exponential growth. In agreement with others (Pumir & Siggia 1990; Kida, Takaoka & Hussain 1991; Shelley & Meiron 1991; Zabusky *et al.* 1991; Boratav *et al.* 1992; Kerr 1993), we observe that the strain rate is maximum off the filament and that vorticity aligns, not with the largest, but with the middle eigenvalue of the strain-rate matrix. This fact suggests that vorticity picking up the largest available, singular-like, strain rate will not be on the filaments themselves. In this sense, bridge formation in vortex reconnection may be low-level vorticity, picking up the very large, off the filament strain-rate growth. Visualizations of the strain rate and vortex stretching fields show that qualitative aspects of direct Navier–Stokes simulations (Kida, Takaoka & Hussain 1991; Zabusky *et al.* 1991; Boratav *et al.* 1992) and the Biot-Savart results are similar. These include the patterns of direction of the eigenvector of the largest eigenvalue α and the normalized vortex stretching (3.22).

Collapse conditions on the density of the motion invariants were suggested by use of a self-similarity ansatz. These conditions, confirmed by the numerical experiments, are such that the line densities, associated with the linear and angular impulse and energy invariants, vanish in the collapsing regions of the vortex filament. The zero-energy-density condition for collapse provides a rational basis for initiating surgery in filament algorithms.

In our multi-filament vortex ring simulations, performed with both constant- and variable-core models and different resolutions, we find that the vorticity of the constant-core model remains nearly constant until the end of the runs. The amplification of the strain rate α_m is moderately faster than that observed for the single-filament case. This amplification saturates as the values of core overlapping in the centre-filament of the ring become $\delta/d_m > 1$. At this time, when large vortex stretching is present, the constant-core model violates the conservation of volume. The saturation is not present in the variable core cases, where the maximum vorticity and strain-rate amplification corresponds to the formation of a smaller-scale vortex structure on the top of the collapse region. The confirmation of the existence of this structure still needs further study at higher resolutions. Quantifications in a cross-section in the collapse region indicate that the circulation tends to concentrate in the upper part of the dipole structure. Also in this region, we have the smallest vortex filament core sizes δ. The strain-rate pattern is similar to that produced by the single-filament case. The main difference is that the lower maximum observed in the single-filament case has vanished. The vortex stretching pattern in the collapse region for the multi-filament case is now closer to the 'torus' shape observed in the continuum simulations.

N. J. Zabusky and V. M. Fernandez acknowledge the facilities provided by the CAIP center at Rutgers University and the recent support of DOE (Grant 93ER25179.A) and ARPA Hypercomputing and Design Contract DABT-63-93-C-0064. V. Fernandez acknowledges partial support of CONACyT-Mexico. V. M. Gryanik acknowledges the support of the National Science Foundation during September-November 1992. Computations were performed on the Cray C90 at the Pittsburgh Supercomputing Center. Some of the multi-filament runs were performed on the CM5 at the National Center for Supercomputing Applications. We are in debt to Ms Pamela Schraedley for editorial assistance.

REFERENCES

Almgren, A. S., Buttke, T. & Colella, P. 1994 A fast adaptive vortex method in three dimensions. *J. Comput. Phys.* **113**, 177–200.

Anderson, C. & Greengard, C. 1985 On vortex methods. *SIAM J. Numer. Anal.* **22**, 413–440.

Anderson, C. & Greengard, C. 1989 The vortex merger problem at infinite Reynolds number. *Commun. Pure Appl. Maths* **42**, 1123–1139.

Arms, R. J. & Hama, F. R. 1965 Localized-Induction concept on a curved vortex and motion of an elliptic vortex ring. *Phys. Fluids* **8**, 553–559.

Ashurst, W. T. & Meiron, D. I. 1987 Numerical study of vortex reconnection. *Phys. Rev. Lett.* **58**, 1632–1635.

Ashurst, W. T., Kerstein, A. R., Kerr, R. M. & Gibson, C. H. 1987 Alignment of vorticity and scalar gradient with strain rate in simulated Navier-Stokes turbulence. *Phys. Fluids* **30**, 2343–2353.

Beale, J. T., Kato, T. & Majda, A. 1984 Remarks on the breakdown of smooth solutions for the 3-D Euler equations. *Commun. Math. Phys.* **94**, 61–66.

Beale, J. T. & Majda, A. 1982 Vortex methods. I: Convergence in three dimensions. *Maths Comput.* **39**, 1–27.

Beale, J. T. & Majda, A. 1985 High order accurate vortex methods with explicit velocity kernels. *J. Comput. Phys.* **58**, 188–208.

Boratav, O. N. & Pelz, R. B. 1994 Direct numerical simulation of transition to turbulence from a high-symmetry initial condition. *Phys. Fluids* A **6**, 2757–2784.

Boratav, O. N., Pelz, R. B. & Zabusky, N. J. 1992 Reconnection in orthogonally interacting vortex tubes: Direct numerical simulations and quantifications. *Phys. Fluids* A **4**, 581–605.

Chen, S.-Y. & Shan, X. 1992 High-Resolution turbulent simulations using the Connection Machine-2. *Computers Phys.* **6**, 643–646.

Chorin, A. J. 1990*a* Vortex filaments and turbulence theory. In *Topological Fluid Dynamics, Proc. IUTAM Symp., Cambridge, August 1989* (ed. H. K. Moffatt & A. Tsinober), pp. 607–616. Cambridge University Press.

Chorin, A. J. 1990*b* Hairpin removal in vortex interactions. *J. Comput. Phys.* **91**, 1–21.

Chorin, A. J. 1993 Hairpin removal in vortex interactions II. *J. Comput. Phys.* **107**, 1–9.

Constantin, P. 1994 Geometric statistics in turbulence. *SIAM Rev.* **36**, 73–98.

Crow, S. C. 1970 Stability theory for a pair of trailing vortices. *AIAA J.* **8**, 2172–2179.

Dhanak, M. R. & Bernardinis, B. de 1981 The evolution of an elliptic vortex ring. *J. Fluid Mech.* **109**, 189–216.

Douady, S. & Couder, Y. 1993 On the dynamical structures observed in 3d turbulence. In *Proc. Workshop on Turbulence in Extended Systems*, Les Houches (ed. R. Benzi, C. Basdevant, S. Ciliberto), pp. 3–17. Nova Science Commack, NY.

Douady, S., Couder, Y. & Brachet, M. E. 1991 Direct observation of the intermittency of intense vorticity filaments in turbulence. *Phys. Rev. Lett.* **67**, 983–986.

Fernandez, V. M. 1994 Vortex intensification and collapse of the Lissajous-Elliptic ring: Biot-Savart simulations and visiometrics. PhD thesis, Rutgers University, New Brunswick, New Jersey.

Fernandez, V. M., Zabusky, N. J. & Gryanik, V. M. 1994 Near-singular collapse and local intensification of a "Lissajous-elliptic" vortex ring: Non-monotonic behavior and zero-approaching local energy densities. *Phys. Fluids* A **6**, 2242–2244.

Fohl, T. & Turner, J. S. 1975 Colliding vortex rings. *Phys. Fluids* **18**, 433–436.

Fukuyu, A. & Arai, T. 1991 Singularity formation in three-dimensional inviscid flow. *Fluid Dyn. Res.* **7**, 229–240.

Greengard, C. 1986 Convergence of the vortex filament method. *Maths Comput.* **47**, 387–398.

Hon, T.-L. & Walker, J. D. A. 1988 Evolution of hairpin vortices in a shear flow. *NASA Tech. Memo.* 100858, ICOMP-88-9.

Hussain, F. & Husain, H. S. 1989 Elliptic jets. Part 1. Characteristics of unexcited and excited jets. *J. Fluid Mech.* **208**, 257–320.

Husain, H. S. & Hussain, F. 1993 Elliptic jets. Part 3. Dynamics of preferred mode coherent structure. *J. Fluid Mech.* **248**, 315–361.

Inoue, O. 1988 Simulation of a vortex ring. *AIAA Paper* 88-3571-CP.

Jiménez, J. 1992 Kinematic alignment effects in turbulent flows. *Phys. Fluids* A **4**, 652–654.

Jimenez, J., Wray, A. A., Saffman, P. G. & Rogallo, R. S. 1993 The structure of intense vorticity in isotropic turbulence. *J. Fluid Mech.* **255**, 65–90.

Johnston, R. T. & Sullivan, J. P. 1994 A flow environment for studying vortex interactions. *Exps. Fluids* **18**, 131.

Kerr, R. M. 1985 Higher-order derivative correlations and the alignment of small-scale structures in isotropic numerical turbulence. *J. Fluid Mech.* **153**, 31–58.

Kerr, R. M. 1987 Histograms of helicity and strain in numerical turbulence. *Phys. Rev. Lett.* **59**, 783–786.

Kerr, R. M. 1993 Evidence for a singularity of the three-dimensional incompressible Euler equations. *Phys. Fluids* A **5**, 1725–1746.

Kerr, R. M. & Hussain, F. 1989 Simulation of vortex reconnection. *Physica* D **37**, 474–484.

Kida, S. & Takaoka, M. 1987 Bridging in vortex reconnection. *Phys. Fluids* **30**, 2911–2914.

Kida, S. & Takaoka, M. 1988 Reconnection of vortex tubes. *Fluid Dyn. Res.* **3**, 257–261.

Kida, S. & Takaoka, M. 1994 Vortex reconnection. *Ann. Rev. Fluid Mech.* **26**, 169–189.

Kida, S., Takaoka, M. & Hussain, F. 1991 Collision of two vortex rings. *J. Fluid Mech.* **230**, 583–646.

Klein, R. & Knio, O. M. 1995 Asymptotic vorticity structure and numerical simulation of slender vortex filaments. *J. Fluid Mech.* **284**, 275–321.

Klein, R. & Majda, A. J. 1991 Self-stretching of perturbed vortex filaments II. Structure of solutions. *Physica* D **53**, 267–294.

Knio, O. M. & Ghoniem, A. F. 1990 Numerical study of a three-dimensional vortex method. *J. Comput. Phys.* **86**, 75–106.

Leonard, A. 1980 Vortex methods for flow simulation. *J. Comput. Phys.* **37**, 289–335.

Leonard, A. 1985 Computing three-dimensional incompressible flows with vortex elements. *Ann. Rev. Fluid Mech.* **17**, 523–559.

Lim, T. T. & Nickels, T. B. 1992 Instability and reconnection in the head-on collision of two vortex rings. *Nature* **357**, 225–227.

Liu, C. H., Tavantzis, J. & Ting, L. 1986 Numerical studies of motion and decay of vortex filaments. *AIAA J.* **24**, 1290–1297.

Maxworthy, T. 1972 The structure and stability of vortex rings. *J. Fluid Mech.* **51**, 15–32.

Meiron, D. I., Shelley, M. J., Ashurst, W. T & Orszag, S. A. 1988 Numerical studies of vortex reconnection. In *Proc. Workshop on Mathematical Aspects of Vortex Dynamics, Leesburg, Virginia* (ed. R. E. Caflisch), pp. 183–194. SIAM.

Melander, M. V. & Hussain, F. 1989 Cross-linking of two antiparallel vortex tubes. *Phys. Fluids* A **1**, 633–636.

Melander, M. V. & Zabusky, N. J. 1988 Interaction and apparent reconnection of 3d vortex tubes via direct numerical simulations. *Fluid Dyn. Res.* **3**, 247–250.

Moore, D. W. 1972 Finite amplitude waves on aircraft trailing vortices. *Aero. Q.* **23**, 307–314.

Oshima, Y. & Asaka, S. 1977 Interaction of two vortex rings along parallel axes in air. *J. Phys. Soc. Japan* **42**, 708–713.

Oshima, Y. & Izutsu, N. 1988 Cross-linking of two vortex rings. *Phys. Fluids* **31**, 2401–2403.

Oshima, Y., Izutsu, N., Oshima, K. & Hussain, A. K. M. F. 1988 Bifurcation of an elliptic vortex ring. *Fluid Dyn. Res.* **3**, 133–139.

Oshima, Y., Noguchi, T. & Oshima, K. 1986 Numerical study of interaction of two vortex rings. *Fluid Dyn. Res.* **1**, 215–227.

Perlman, M. 1985 On the accuracy of vortex methods. *J. Comput. Phys.* **59**, 200–223.

Ponce, G. 1985 Remarks on a paper by J. T. Beale, T. Kato and A. Majda. *Commun. Math. Phys.* **98**, 349–353.

Pumir, A. & Kerr, R. M. 1987 Numerical simulation of interacting vortex tubes. *Phys. Rev. Lett.* **58**, 1636–1639.

Pumir, A. & Siggia, E. D. 1987 Vortex dynamics and the existence of solutions to the Navier-Stokes equations. *Phys. Fluids* **30**, 1606–1626.

Pumir, A. & Siggia, E. 1989 Simulations of incipient singularities in the 3-D Euler equations. *Physica* D **37**, 539–541.

PUMIR, A. & SIGGIA, E. 1990 Collapsing solutions to the 3-D Euler equations. *Phys. Fluids* A **2**, 220–241.

ROBINSON, S. K. 1991 Coherent motions in the turbulent boundary layer. *Ann. Rev. Fluid Mech.* **23**, 601–639.

SAFFMAN, P. G. 1970 The velocity of viscous rings. *Stud. Appl. Maths* **49**, 371–380.

SCHATZLE, P. R. 1987 An experimental study of fusion of vortex rings. PhD thesis, California Institute of Technology, Pasadena, California.

SHE, Z.-S., JACKSON, E. & ORSZAG, S. A. 1990*a* Intermittent vortex structures in homogeneous isotropic turbulence. *Nature* **344**, 226–228.

SHE, Z.-S., JACKSON, E. & ORSZAG, S. A. 1990*b* Vortex structure and dynamics in turbulence. *Computer Meth. Appl. Mech. Engng* **80**, 173–183.

SHE, Z.-S., JACKSON, E. & ORSZAG, S. A. 1991 Structure and dynamics of homogeneous turbulence: Models and simulations. *Proc. R. Soc. Lond.* A **434**, 101–124.

SHELLEY, M. J. & MEIRON, D. I. 1991 *Vortex reconnection and smoothness of the Euler equations.* Lectures in Applied Mathematics, vol. 26, pp. 647–677. Springer.

SHELLEY, M. J., MEIRON, D. I. & ORSZAG, S. A. 1993 Dynamical aspects of vortex reconnection of perturbed anti-parallel vortex tubes. *J. Fluid Mech.* **246**, 613–652.

SIGGIA, E. D. 1981 Numerical study of small-scale intermittency in three-dimensional turbulence. *J. Fluid Mech.* **107**, 375–406.

SIGGIA, E. D. 1985 Collapse and amplification of a vortex filament. *Phys. Fluids* **28**, 794–805.

SIGGIA, E. D. & PUMIR, A. 1985 Incipient singularities in the Navier-Stokes equations. *Phys. Rev. Lett.* **55**, 1749–1752.

SMITH, G. B. 1992 Turbulent cascade to small scales during the off-axis collision of two vortex rings. MS thesis, Rutgers University, Graduate Program in Mechanical and Aerospace Engineering.

SMITH, G. B. & WEI, T. 1994 Small-scale structure in colliding off-axis vortex rings. *J. Fluid Mech.* **259**, 281–290.

TING, L. & KLEIN, R. 1991 *Viscous Vortical Flows.* Lecture Notes in Physics, vol. 374, section 2.4, pp. 103–115. Springer

VINCENT, A. & MENEGUZZI, M. 1991 The spatial structure and statistical properties of homogeneous turbulence. *J. Fluid Mech.* **225**, 1–20.

VINCENT, A. & MENEGUZZI, M. 1994 The dynamics of vorticity tubes in homogeneous turbulence. *J. Fluid Mech.* **258**, 245–254.

WAELE, A. T. M. M. DE & AARTS, R. G. K. M. 1994 Route to vortex reconnection. *Phys. Rev. Lett.* **72**, 482–485.

WIDNALL, S. E., BLISS, D. B. & TSAI, C.-Y. 1974 The instability of short waves on a vortex ring. *J. Fluid Mech.* **66**, 35–47.

WIDNALL, S. E. & SULLIVAN, J. P. 1973 On the stability of vortex rings. *Proc. R. Soc. Lond.* A **332**, 335–353.

WINCKELMANS, G. S. 1989 Topics in vortex methods for the computation of three- and two-dimensional incompressible unsteady flows. PhD thesis, California Institute of Technology, Pasadena, California.

WINCKELMANS, G. S. & LEONARD, A. 1993 Contributions to vortex particle methods for the computation of three-dimensional incompressible unsteady flows. *J. Comput. Phys.* **109**, 247–273.

ZABUSKY, N. J., BORATAV, O. N., PELZ, R. B., GAO, M., SILVER, D. & COOPER, S. P. 1991 Emergence of coherent patterns of vortex stretching during reconnection: A scattering paradigm. *Phys. Rev. Lett.* **67**, 2469–2472.

ZABUSKY, N. J. & MELANDER, M. V. 1989 Three-dimensional vortex tube reconnection: Morphology for orthogonally-offset tubes. *Physica* D **37**, 555–562.

ZABUSKY, N. J., SILVER, D. & PELZ, R. 1993 Visiometrics, juxtaposition and modeling. *Phys. Today* **46**, 24–31.

ZAKHAROV, V. E. 1988 Wave collapse. *Sov. Phys. Usp.* **31**, 672–674.